Plant Physiology and Biochemistry 207 (2024) 108365

Contents lists available at ScienceDirect

Plant Physiology and Biochemistry

journal homepage: www.elsevier.com/locate/plaphy

Dynamic adaptation of the extremophilic red microalga *Cyanidioschyzon merolae* to high nickel stress

Francesca Marchetto [a], Sergio Santaeufemia [a], Magdalena Lebiedzińska-Arciszewska [b], Małgorzata A. Śliwińska [c], Magdalena Pich [d], Eliza Kurek [d], Aleksandra Naziębło [e], Marcin Strawski [f], Daniel Solymosi [g], Marek Szklarczyk [f], Ewa Bulska [d], Jędrzej Szymański [c], Małgorzata Wierzbicka [e], Yagut Allahverdiyeva [g], Mariusz R. Więckowski [b], Joanna Kargul [a,*,1]

[a] *Solar Fuels Laboratory, Center of New Technologies, University of Warsaw, 02-097, Warsaw, Poland*
[b] *Laboratory of Mitochondrial Biology and Metabolism, Nencki Institute of Experimental Biology PAS, Warsaw, Poland*
[c] *Laboratory of Imaging Tissue Structure and Function, Nencki Institute of Experimental Biology PAS, 02-093, Warsaw, Poland*
[d] *Biological and Chemical Research Center, Faculty of Chemistry, University of Warsaw, 02-089, Warsaw, Poland*
[e] *Laboratory of Ecotoxicology, Institute of Botany, Faculty of Biology, University of Warsaw, 02-089, Warsaw, Poland*
[f] *Laboratory of Electrochemistry, Faculty of Chemistry, University of Warsaw, 02-089, Warsaw, Poland*
[g] *Molecular Plant Biology Unit, Department of Life Technologies, University of Turku, Turku, FI-20014, Finland*

ARTICLE INFO

Handling Editor: Dr. Mario De Tullio

Keywords:
Abiotic stress
Adaptation
Cyanidioschyzon merolae
Heavy metals
Nickel
Photosynthesis and respiration

ABSTRACT

The order of Cyanidiales comprises seven acido-thermophilic red microalgal species thriving in hot springs of volcanic origin characterized by extremely low pH, moderately high temperatures and the presence of high concentrations of sulphites and heavy metals that are prohibitive for most other organisms. Little is known about the physiological processes underlying the long-term adaptation of these extremophiles to such hostile environments. Here, we investigated the long-term adaptive responses of a red microalga *Cyanidioschyzon merolae*, a representative of Cyanidiales, to extremely high nickel concentrations. By the comprehensive physiological, microscopic and elemental analyses we dissected the key physiological processes underlying the long-term adaptation of this model extremophile to high Ni exposure. These include: (*i*) prevention of significant Ni accumulation inside the cells; (*ii*) activation of the photoprotective response of non-photochemical quenching; (*iii*) significant changes of the chloroplast ultrastructure associated with the formation of prolamellar bodies and plastoglobuli together with loosening of the thylakoid membranes; (*iv*) activation of ROS amelioration machinery; and (*v*) maintaining the efficient respiratory chain functionality. The dynamically regulated processes identified in this study are discussed in the context of the mechanisms driving the remarkable adaptability of *C. merolae* to extremely high Ni levels exceeding by several orders of magnitude those found in the natural environment of the microalga. The processes identified in this study provide a solid basis for the future investigation of the specific molecular components and pathways involved in the adaptation of Cyanidiales to the extremely high Ni concentrations.

1. Introduction

Dissecting the intricacies of homeostasis regulation in extremophilic organisms is pivotal for understanding the boundaries where life can flourish and shedding light on its origin. Different species of extremophiles inhabit environments that are hostile for most forms of life. Among those, particularly fascinating is the rhodophytan order of Cyanidiales that comprises seven species of extremophilic red microalgae thriving in acidic hot springs of volcanic origin. The abiotic conditions of such environments include very low pH (0.05–4), moderately high temperatures (40–57 °C) as well as the presence of sulphites and heavy metals at concentrations that are prohibitive for most other forms

* Corresponding author.
E-mail address: j.kargul@cent.uw.edu.pl (J. Kargul).
[1] The author responsible for the distribution of materials integral to the findings presented in this article following the policy described in the Guide for Authors (https://www.elsevier.com/journals/plant-physiology-and-biochemistry/0981-9428/guide-for-authors) is Joanna Kargul (j.kargul@cent.uw.edu.pl)

https://doi.org/10.1016/j.plaphy.2024.108365
Received 28 July 2023; Received in revised form 23 December 2023; Accepted 10 January 2024
Available online 11 January 2024

of life and are significantly higher than those permitted by the international toxicity regulating bodies. As an example, concentrations of 0.058, 0.023, 0.571 ppm of Ni, Cd and Cr, respectively, have been found in the natural environments of Cyanidiales (Shakhatreh et al., 2017), which are 3-11-fold higher than the limits set by the World Health Organization (0.02, 0.003 and 0.05 ppm for Ni, Cd and Cr, respectively; Carr and Neary, 2008; Luca et al., 1978).

One of the most studied Cyanidiales species is *Cyanidioschyzon merolae*, a unicellular thermo-acidophilic red microalga, isolated from volcanic hot springs in Campi Flegrei, Naples, Italy (Luca et al., 1978). This organism has attracted a great deal of interest because of its evolutionary position at the root of the red algal lineage (Miyagishima et al., 2017). It has been considered an evolutionary link between prokaryotic cyanobacteria and photosynthetic eukaryotes. One of the most striking features of *C. merolae* is the hybrid character of its photosynthetic apparatus, as shown by the presence of cyanobacterial-like photosystem II (PSII) with associated phycobilisomes (PBS) serving as the light harvesting antennae containing *c*-phycocyanin and allophycocyanin as the main pigments. The photosystem I (PSI) complex is of a eukaryotic type, containing the LHCI antenna associated asymmetrically with the core complex on the PsaF/PsaJ side. Both photosystems (PS) contain exclusively chlorophyll *a* (Chl *a*) in contrast to the much richer composition of Chl species in other phototrophs.

The cell structure of *C. merolae* is very simple, with only a single nucleus, a single mitochondrion and a single chloroplast. Noteworthy, *C. merolae*, in contrast to other Cyanidiales, does not contain the cell wall or typical vacuoles, although electron-dense bodies of single membrane-bound, vacuole-like organelles rich in polyphosphate have been identified (Yagisawa et al., 2009). All the three genomes of *C. merolae* are fully sequenced, making this microalga an attractive model system to dissect the evolution and molecular components of the signalling pathways related to the fundamental cellular processes including oxygenic photosynthesis, cell cycle, cell division, protein and lipid homeostasis and circadian rhythms (reviewed in Miyagishima and Tanaka, 2021 and references therein).

To date, the in-depth understanding of the long-term physiological responses of Cyanidiales to severe stressors such as high concentrations of heavy metals, high temperatures, high light and extremely acidic pH remains limited. Despite a plethora of evidence pointing towards the adaptability of Cyanidiales to elevated levels of heavy metals (Varshney et al., 2015), little is known about the precise molecular mechanisms underlying the heavy metal defence and detoxification strategies or the effects of heavy metals on the structure and function of the photosynthetic apparatus in these fascinating photosynthetic extremophiles that drive the primary biomass production in the hot environments rich in heavy metals and high salt.

The main objective of this study was to provide a comprehensive insight into the long-term adaptation mechanisms of *C. merolae* cells to high concentrations of heavy metals, specifically nickel. By combining advanced spectroscopic, microscopic and elemental analyses we demonstrate the remarkable adaptability of *C. merolae* to extremely high (mM) concentrations of this heavy metal, with the concomitant preservation of high cell viability, amelioration of reactive oxygen species (ROS), high photosynthetic performance, the presence of the efficient photoprotective mechanisms, and dynamic reorganization of the thylakoid architecture.

2. Materials and Methods

2.1. Cell culturing, cell growth measurement and IC_{50}

Cyanidioschyzon merolae strain NIES-3377 and *Chlamydomonas reinhardtii* strain NIES-2237 (obtained from the Microbial Culture Collection of the National Institute for Environmental Studies in Japan) were cultivated in a modified Allen-2 medium (Allen, 1959) at 42 °C, pH 2.5 (Minoda et al., 2004) or in TAP medium pH 7.2 at 20 °C (Harris, 1989), respectively, with continuous shaking at 110 rpm. Cell suspensions (125 mL) were grown in glass conical flasks (Duran®) in continuous white light of 90 μE m^{-2} s^{-1} using an FL40SS-ENW/37H growth chamber (Panasonic) for *C. merolae* and under 70 μE m^{-2} s^{-1} of continuous white light using LED-illuminated chamber (Biogenet) for *C. reinhardtii*. The Ni stock solution was prepared by adding $NiSO_4$ x $6H_2O$ in MilliQ water to obtain a final concentration of 200 g L^{-1}. An appropriate volume of Allen-2 medium, *C. merolae* stock culture and Ni stock solution was added to each flask to obtain a final concentration of 1, 3, 6 and 10 mM Ni. In the case of *C. reinhardtii,* TAP medium, algae donor culture and Ni stock solution were added to each flask to reach the final concentration of 0.1 and 0.2 mM Ni. The control culture was prepared using the same procedure but omitting the Ni solution. Ni adaptation experiments were carried out for a final period of 15 days. Exponentially growing cells were employed for all experiments, with a starting OD_{750} ~0.15. For all the timepoints and Ni concentrations investigated in the study, the samples were analysed in parallel during the same measurements using two independent biological replicas (n = 2). Cell growth was monitored daily by recording room temperature (RT) absorption spectra in the range of 370–750 nm and recording the values of OD_{750} using a UV-1800 spectrophotometer (Shimadzu).

The IC_{50} values, at which the growth of *C. merolae* is inhibited by 50% compared to untreated cells, were obtained for each Ni concentration at day 15. The IC_{50} value was calculated using OriginPro software (OriginLab Corporation, 2018) through nonlinear curve Dose/Response. The growth inhibition percentage was calculated according to Eq. (1) using OD_{750} values after 15 days of growth of the two biological replicas for each Ni treatment (Monteiro et al., 2011).

$$Growth\ inhibition\ (\%) = \frac{OD_{750}\ Untreated\ cells\ -\ OD_{750}\ Treated\ cells}{OD_{750}\ Untreated\ cells} \times 100 \quad \text{(Eq. 1)}$$

2.2. Confocal fluorescence imaging

For confocal imaging sample preparation, an aliquot of cell suspension (10 μL) was dispensed onto the 2% agar squares of 0.75 mm thickness placed on the microscopic slides, then covered with a coverslip. Confocal imaging of the cells was performed using an LSM700 confocal laser scanning microscope (Zeiss) at 63× magnification. The average size of chloroplasts (measured along the longest axis) was estimated for at least 50 cells for each of the two independent biological replicas. Two channels were simultaneously used to visualize PSI and PSII (excitation at 488 nm and fluorescence emission at 516 nm) or PBS complexes (excitation at 555 nm and fluorescence emission at 585 nm). To determine the cell viability a dual laser beam setup was used, as described in Millach et al. (2019). Firstly, a red channel (excitation at 555 nm and fluorescence emission at 573 nm) was employed to observe viable cells and the chloroplast autofluorescence signal. Simultaneously, a green channel (excitation at 405 nm and fluorescence emission at 435 nm) was applied to visualize non-viable cells and the autofluorescence signal from non-photosynthetic components. Four different micrographs were acquired for every biological sample. At least 80 cells were evaluated for cell viability for each independent biological sample. Cell counting and statistical analyses were performed to determine the exact number of viable and non-viable cells in the culture exposed to each Ni concentration.

2.3. Pigment quantification

For the total Car and Chl *a* quantification, pigments were extracted from the cells using ultrapure (≥99.8%) N,N-dimethylformamide (DMF). Briefly, an aliquot of cell suspension was centrifuged for 10 min at 14,000 g. After the removal of the supernatant, 1 mL DMF was mixed vigorously with the cell pellet, then incubated in the dark at −20 °C for 24 h for total pigment extraction. The samples were then

centrifuged for 10 min at 14,000 g. Room temperature (RT) absorption spectra of pigment extracts were measured in the range of 350–750 nm using a UV-1800 spectrophotometer (Shimadzu) and ultrapure DMF as blank. The concentration of pigments (μg mL^{-1}) in the cellular extract was calculated according to Eqs. (1) and (2) taking into consideration the dilution factor (Dil) and the ratio between the volume of the sample (V_{sample}, mL) and the volume of DMF (V_{DMF}, mL) used to extract the pigments (Borella et al., 2022; Wellburn, 1994):

$$[Chl\ a] = (A_{664} - A_{750}) \times 11.92 \times Dil \times \frac{V_{DMF}}{V_{sample}} \quad \text{(Eq. 2)}$$

$$[Car] = \frac{[(1000\ x\ A_{480}) - (0.89\ x\ Chla)]}{245} \times Dil \times \frac{V_{DMF}}{V_{sample}} \quad \text{(Eq. 3)}$$

where A is the absorbance at an indicated wavelength. The pigment content (pg mL^{-1}) was normalized to the number of cells per mL, as determined with a hemocytometer (Burker), and expressed as % control. Extinction coefficients for Chl *a* and Car in DMF were 83.9 L g^{-1} cm^{-1} (Moran, 1982) and 2500 L g^{-1} cm^{-1}, respectively (Hirschberg and Chamovitz, 1994).

2.4. Absorption spectroscopy

RT absorption spectra were acquired in a range of 350–750 nm with a 10 mm-optical path length using a UV-1800 spectrophotometer (Shimadzu) supplied with a TCC-100 temperature-controlled cell holder.

2.5. 77K fluorescence spectroscopy

Steady-state fluorescence emission spectra of intact cells (2 μg Chl) were measured at 77K using an LS55 Fluorescence Spectrometer (Perkin Elmer), as described by Krupnik et al. (2013). Emission spectra of PSII, PSI and PBS complexes were recorded using excitation wavelengths of 435 and 600 nm, respectively. The emission spectra were normalized to the PSII peak (685 nm). Each spectrum was obtained from the average of two independent biological replicas.

2.6. ROS production measurement

To measure ROS production rates *in vivo*, 2′,7′-dichlorodihydrofluorescein diacetate (DCF; excitation/emission ranges: 492–495/517–527 nm) was used as an internal fluorescent probe by appropriate dilution of freshly made 5 mM stock solution of the probe in dimethyl sulfoxide (DMSO). In parallel, an aliquot (3 mL) of *C. merolae* cell suspension was centrifuged for 8 min at 1000 g and the supernatant was removed. The pellet was then resuspended in 3.5 mL of phosphate buffered saline (sodium chloride, 145 mM (0.85%) in phosphate buffer, 150 mM) (pH 7.0) at 30 °C. An aliquot (6.5 μl) of DCF stock solution was added to the final concentration of 9.3 μM and the sample was gently mixed. Cell suspensions (0.25 mL) were then transferred to a 48-well microplate. Fluorescence of the oxidized DCF probe was measured using an Infinite M200 plate reader (TECAN, Männedorf, Switzerland) in real time for a total period of 65 min. The quantitative fluorescence data was processed with a Magellan™ software (TECAN). Total protein content was measured using a Bradford assay (Bradford, 1976). Briefly, 0.2 mL of cell suspension was mixed with 0.05 mL of 100 mM NaOH, 0.3 mL of the Bradford reagent and 1 mL of water in a 1.5 ml cuvette. Absorbance at 595 nm was measured and protein content was determined using freshly prepared calibration curves and bovine serum albumin as a standard. Protein content (mg mL^{-1}) was calculated considering a 1-cm optical path length and the extinction coefficient of 6.6 $(g/100\ mL)^{-1}$ cm^{-1}. The ROS production rate, determined for 2 biological replicas with 6 technical replicas for each biological sample, was normalized to the protein concentration in the sample volume. To achieve the highest accuracy of the ROS production measurements, the protein concentration was measured precisely in the cell suspension prior to adding the corresponding sample (on an equal volume basis) to the individual wells in the multiwell plate used for the ROS assay.

2.7. Oxygen evolution and consumption measurement

A Clark-type electrode (Hansatech) was used to determine net oxygen evolution and consumption rates in cell suspensions. Measurements were performed at 30 °C using a freshly calibrated electrode. The sample (1 mL) was preincubated in the dark with gentle stirring for 25 min after which net oxygen consumption rate (nmol O_2 h^{-1}) was measured. The sample was then illuminated for 15 min at 2000 μE m^{-2} s^{-1} using a KL 2500 LED light box (Schott) to measure the oxygen evolution rate (nmol O_2 h^{-1}). The values were then normalized to 10^6 cells per mL, and expressed as % control. The total cell number was determined for each sample using a hemocytometer (Burker). For the oxygen consumption measurements in the presence of 23.1 μM 2,4-dinitrophenol (DNP), 1 mL sample was dark adapted for 15 min after which the oxygen consumption rate (nmol O_2 h^{-1}) was measured. To determine the effective concentration of DNP for uncoupling the oxidative phosphorylation from the mitochondrial electron transport chain 100 μL aliquots of 0.1 mM DNP stock solution was added **to each cell suspension** sample in the dark every 10 min and the oxygen consumption rate (nmol O_2 h^{-1}) was measured immediately. The values were normalized to 10^6 cells per mL and expressed as % control.

2.8. DUAL-PAM measurement

To measure the photosynthetic performance parameters, pulse-amplitude-modulated fluorescence spectra were recorded and analysed using a DUAL-PAM 100 fluorimeter (Heinz Walz Gmbh, Germany) and a DUAL-PAM v1.19 software. An aliquot (1 mL) of cell suspension was placed in a 10 mm quartz cuvette supplemented with a magnetic stirrer and incubated for 10 min in the dark. Then, an actinic pulse (12 μE m^{-2} s^{-1}) was applied to record the minimal fluorescence (F_o: the fluorescence yield of the open reaction centers of PSII, after dark adaptation). The maximum fluorescence yield of PSII (F_m) was then recorded by applying a saturation pulse (SP) of 4000 μE m^{-2} s^{-1} for 300 ms at 620 nm. Maximum quantum yield of PSII (F_v/F_m), was calculated using Equation (4):

$$F_v \Big/ F_m = \frac{(F_m - F_o)}{F_m} \quad (4)$$

To quantify $P700^+$ signal a dual wavelength unit (830/875 nm) was used to record simultaneously the changes in absorption at 700 nm (Klughammer and Schreiber, 1994). P_m, defined as the maximal P700 change, was detected after application of a far-red light pulse at 720 nm for 10 s, followed by a SP. For recording the Slow Kinetics Curves, a blue actinic light pulse of 90 μE m^{-2} s^{-1} was used followed by SPs applied every 30 s until a steady state was achieved. For each SP, the values of F_m' and P_m' (maximum PSII fluorescence yield and maximum change of the P700 signal in a given light, respectively; see Eqs. (5)–(7)), was recorded. Then, the actinic light (Blue Light; λ = 460 nm) was switched off. Effective quantum yields of PSII (Y(II)) and PSI (Y(I)) and non-regulated energy dissipation yield (Y(NO)) were calculated using the following equations:

$$Y(II) = \frac{(F_m' - F)}{F_m'} \quad (5)$$

$$Y(I) = \frac{(P_m' - P)}{P_m} \quad (6)$$

$$Y(NO) = \frac{F}{F_m'} \quad (7)$$

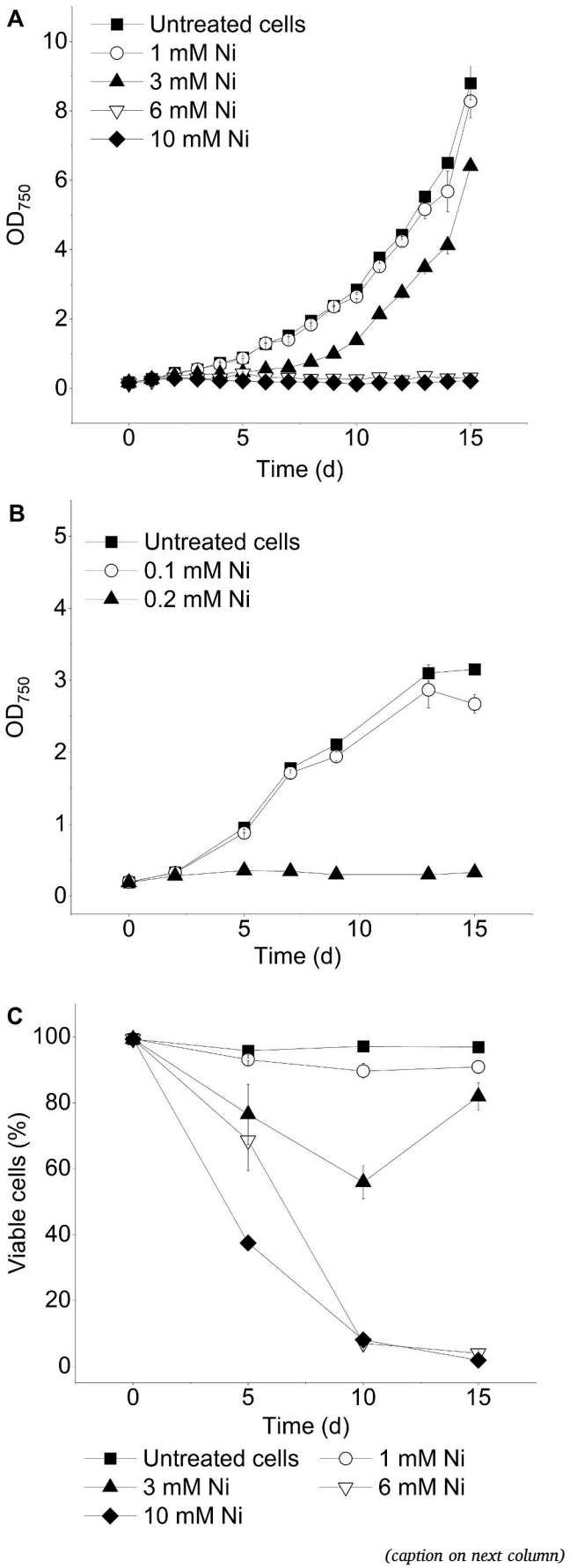

(caption on next column)

Fig. 1. Growth curves and viability of *C. merolae* and *C. reinhardtii* cells exposed to various nickel concentrations. *C. merolae* (A) and *C. reinhardtii* (B) cell growth was assessed by measuring OD_{750} values of cell suspensions during up to 15-day exposure to 0.1–10 mM Ni. Data in (A–B) represents the mean ± SD of two independent biological replicas (n = 2). (C) Cell viability assessment by confocal fluorescence imaging. Dual Laser measurements by CLSM were performed following the protocol by Millach et al. (2019). For each timepoint the viable cells were counted and the percentage of living cells in the whole cell population was calculated, and the corresponding viability data, shown in (C), represents the mean ± SD of two independent biological replicas (n = 2).

where Y(II), and Y(NO) are the effective quantum yield of PSII and the quantum yield of non-regulated energy dissipation, respectively, while Y (I) corresponds to the effective quantum yield of PSI. Besides, F is the fluorescence emission; P is the signal from the PSI reaction center before the application of the saturation pulse.

2.9. Measurement of NPQ kinetics

The non-photochemical quenching (NPQ) was measured using a DUAL-PAM 100 fluorometer (Heinz Walz GmbH, Germany) by applying a standard procedure used for cyanobacteria, as described in Canonico et al. (2020). Cells were dark adapted for 10 min with gentle stirring prior to the measurements. The F_m values of dark-adapted samples were registered by applying a saturating pulse (4000 μE m^{-2} s^{-1}, 400 ms, λ = 620 nm). After 120 s of dark adaptation the cells were subjected to a low intensity blue light illumination (90 μE photons m^{-2} s^{-1}, λ = 460 nm). After 120 s the blue light intensity was increased to 1500 μE m^{-2} s^{-1}, λ = 460 nm) for 200 s. A recovery phase was recorded whereby the actinic light intensity was decreased (90 μE m^{-2} s^{-1}, λ = 460 nm). The maximal value of fluorescence was estimated by a multiple turnover flash (red light λ = 620 nm, 4000 μE m^{-2} s^{-1}, duration 400 ms) every 30 s.

2.10. Inductively Coupled Plasma Mass Spectrometry (ICP-MS) analysis

Aliquots of cell suspensions (50 mL) were collected at different timepoints (6 h, and 5, 10 and 15 days) and centrifuged for 20 min at 2500 g at 4 °C. The supernatant (growth medium) was removed and the cell pellet was immediately processed for ICP-MS analysis. Alternatively, cell pellets were resuspended in a 2 mL aliquot of 0.05% SDS and 0.05 M 1,4-dithiothreitol, then boiled for 5 min and immediately used for ICP-MS analysis. An inductively coupled plasma mass spectrometer (NexION 300D ICP Mass Spectrometer, Perkin Elmer SCIEX, USA) was used. A conventional Mainhardt nebulizer and a quartz cyclonic spray chamber were used for sample introduction. Nickel content was determined by monitoring the ^{61}Ni isotope. The background interferences from the plasma gases, air entrainment and solvent were corrected by subtraction of reagent blank signals. For sample dilution and preparation of standards ultrapure water (MilliQ, Millipore) and nitric acid (HNO_3, Sigma Aldrich) were used. The reagent blank solution contained 1% of concentrated HNO_3. Single standard solution containing Ni was prepared in reagent blank solutions. External calibration was performed with the standard solutions containing 0.1 μg L^{-1}, 1 μg L^{-1}, 10 μg L^{-1}, 100 μg L^{-1} of nickel. The limit of detection for nickel was 0.1 μg L^{-1}. The ICP-MS conditions are shown below.

Parameters	Value
Nebulizer Gas Flow	0.83 L min^{-1}
Auxiliary Gas Flow	1.15 L min^{-1}
Plasma Gas Flow	16.00 L min^{-1}
ICP RF Power	1350 W
Spray chamber	quartz type Scott
Sample cone	Nickel
Skimmer cone	Nickel

2.11. Time-of-Flight Secondary Ion Mass Spectrometry

Time-of-Flight Secondary Ion Mass Spectrometry (TOF-SIMS) analysis was performed using a TOF-SIMS 5 spectrometer (IONTOF GmBH, Germany). To obtain good horizontal resolution and at the same time high spectral resolution, delayed extraction mode was used. The bismuth ion source was used operating at conditions: Bi_3^+, 30 keV, ion current: 0.08–0.12 pA over 50 × 50 μm^2 area rastered at a resolution of 256 × 256 pixels. Mass spectra were monitored up to the m/z value of 900 and were internally calibrated using Na^+, Si^+, $C_3H_4^+$, $C_3H_5^+$, $C_4H_7^+$ and $C_5H_9^+$ ions. Two protocols of sample preparation for SIMS-TOF measurements were applied: (*i*) sample with cells placed in 2-Allen and Ni^{2+} solution after placing on silicon wafer was evaporated and then placed in SIMS-TOF chamber, or (*ii*) sample, before placing on silicon wafer, was washed in a single step using the following procedure: cells were centrifuged for 5 min at 268×*g* at 21 °C, then resuspended in 2-Allen medium without Ni^{2+} ions. A 5 μl volume of the cell suspension was subsequently placed on the silicon surface. After solvent evaporation the samples were immediately analysed.

2.12. Scanning Electron Microscopy with Energy Dispersive spectroscopy analysis

For sample preparation, cells were collected and gently mixed with 8% DMSO. A 10 μL aliquot of cell suspension was placed on a carbon disk attached to the aluminium sample platform (12.7 mm in diameter) and placed in the oven at 70 °C for 15 min until the samples were completely dried. The samples were then analysed by Scanning Electron Microscopy combined with Energy Dispersive X-ray Spectroscopy (SEM-EDS) using a ProX X-ray spectroscope (Phenom).

2.13. Transmission Electron Microscopy imaging

For Transmission Electron Microscopy (TEM) analysis, cells were prefixed with 1% glutaraldehyde in 10 mM sodium cacodylate buffer (pH 7.2). The fixative was added directly to the growth medium at a 1:1 ratio. After 2-h incubation at RT, two washing steps with 10 mM cacodylate buffer were applied. Cells were then immobilized in 2% agarose, post-fixed with 1% osmium tetroxide and 1.5% potassium ferrocyanide, exposed to 1% aqueous thiocarbohydrazide, 2% osmium tetroxide followed by *en bloc* staining with 1% aqueous uranyl acetate and 0.66% lead aspartate. Cells were dehydrated by applying increasing ethanol concentrations (30−100% range), then embedded in epoxy resin, and cut into thin sections (65 nm) using an Ultracut R ultramicrotome (Leica Microsystems, Vienna, Austria). Grids with sections were examined with a JEM 1400 (JEOL Co., Tokyo, Japan, 2008) TEM microscope, equipped with an 11-megapixel TEM camera MORADA G2 (EMSIS GmbH, Münster, Germany).

2.14. Statistical analysis

All measurements were performed in two biological replicas and are reported as mean values ± SD. When technical replicas are used they are specified where appropriate. ANOVA test (Analysis of Variance) and post-hoc Siegel Tukey test were performed using a RStudio Team software (RStudio Team, 2015). Values with $p < 0.05$ were considered significantly different. All the graphs were prepared using an OriginPro software (OriginLab Corporation, 2018).

3. Results and discussion

3.1. Growth and viability of C. merolae cells in presence of high concentrations of nickel

As the starting point of our study, we determined the growth curves of *C. merolae* cells exposed to 1, 3, 6 and 10 mM Ni concentrations (58.6, 175.8, 351.6 and 586 ppm, respectively) for up to 15 days (Fig. 1A). The Ni concentrations applied in our study are up to 7 orders of magnitude higher than those reported for the majority of aquatic environments. For instance, Ni concentrations of 2.33×10^{-6} mM or 1.70×10^{-8} mM have been found in seawater (Kremling and Pohl, 1989) and freshwater (Eisler, 1998) environments, respectively. On the other hand, the Ni concentration in the hot volcanic springs from which *C. merolae* was isolated is in the range of 0.2–9.1 ppm, which corresponds to 0.003–0.155 mM Ni (Piochi et al., 2019). Therefore, it is likely that *C. merolae* may have evolved efficient adaptation mechanisms that allow this alga to thrive in the Ni-rich environments, including the anthropogenically polluted environments.

We observed that up to 1 mM Ni in the growth medium, no significant decrease in cell growth occurred compared to the control ($p < 0.05$ for day 5, 10 and 15; Fig. 1A), which confirms the adaptability of *C. merolae* to high Ni concentrations applied in the mM range. On the other hand, cultures exposed to Ni concentrations higher than 1 mM, i.e., 3, 6 and 10 mM, showed gradual inhibition of cell growth from day 2 of the treatment compared to the untreated cells ($p < 0.0001$). This inhibitory effect was especially severe in the case of 6 mM and 10 mM Ni treatment, whereby the optical density at 750 nm (OD_{750}) significantly decreased after 5 days of Ni exposure. However, in the case of 3 mM Ni, dynamic cell growth was observed in the first 3 days followed by a lag phase until day 5 and logarithmic growth from day 6 until day 15 (last day of the experiment), albeit with a slower growth rate compared to the control and cells exposed to 1 mM Ni ($p < 0.01$). The measurement of room temperature (RT) absorption spectra of cell suspensions (Fig. S1) confirmed the same dynamics of cell growth recovery as observed in growth curves. The observed cell growth recovery at 3 mM Ni indicates triggering the adaptation mechanisms in *C. merolae* cells that allow these cells to thrive in the presence of such highly toxic concentrations of Ni. The fitting of the growth data of *C. merolae* in the presence of different Ni concentrations allowed us to determine the IC_{50} value of 3.94 mM Ni on day 15 corresponding to Ni concentration at which cell growth (monitored at OD_{750}) is reduced by 50% (Fig. S2).

These results were compared with the growth dynamics of the mesophilic green microalga *Chlamydomonas reinhardtii*, which inhabits environments of neutral pH and temperatures around 20–32 °C. Growth of *C. reinhardtii* cells exposed even to 0.2 mM Ni was inhibited in the first 24 h of the treatment, compared to the untreated control (Fig. 1B). In contrast, *C. reinhardtii* cells exposed to 0.1 mM Ni showed similar growth to untreated cells during the 15-day experiment. This data is in line with the study of Zheng et al. (2013), where the growth of *C. reinhardtii* exposed to Ni concentrations between 0.125 and 0.150 mM decreased considerably, whereas it was largely unaffected at Ni concentrations between 0.03 and 0.09 mM. These results confirm the high adaptability of *C. merolae* to concentrations of Ni that are at least an order of magnitude higher compared to those tolerated by microalgae present in neutral environments such as *C. reinhardtii*.

Cellular viability assessment by confocal microscopy allowed us to estimate the proportion of living cells present in the cell population exposed to 1–10 mM Ni (Fig. 1C). In the case of 1 mM Ni, the number of viable cells remained nearly constant (~90%) throughout the experiment, reaching a viability of ~91% on day 15, which was somewhat lower than the proportion of viable control cells (~97%). On day 5 and later, significant differences were observed between the untreated cells and cells exposed to Ni concentrations above 1 mM: this difference was most noticeable on day 15 ($p < 0.01$), where the proportion of viable cells exposed to 6 mM and 10 mM Ni was a mere 4% and 2%, respectively. Interestingly, we observed the recovery of cell viability in the case of 3 mM Ni samples, i.e. from 56% on day 10 to 82% on day 15 (Fig. 1C) confirming the capability of *C. merolae* to adapt to such high Ni concentrations. The cell viability data upon exposure up to 3 mM Ni is in line with the OD_{750} data, where cell growth recovery was observed. In contrast to the resilience of *C. merolae* to the mM Ni treatment, growth of mesophilic green microlalgae *Chlamydomonas vulgaris* and

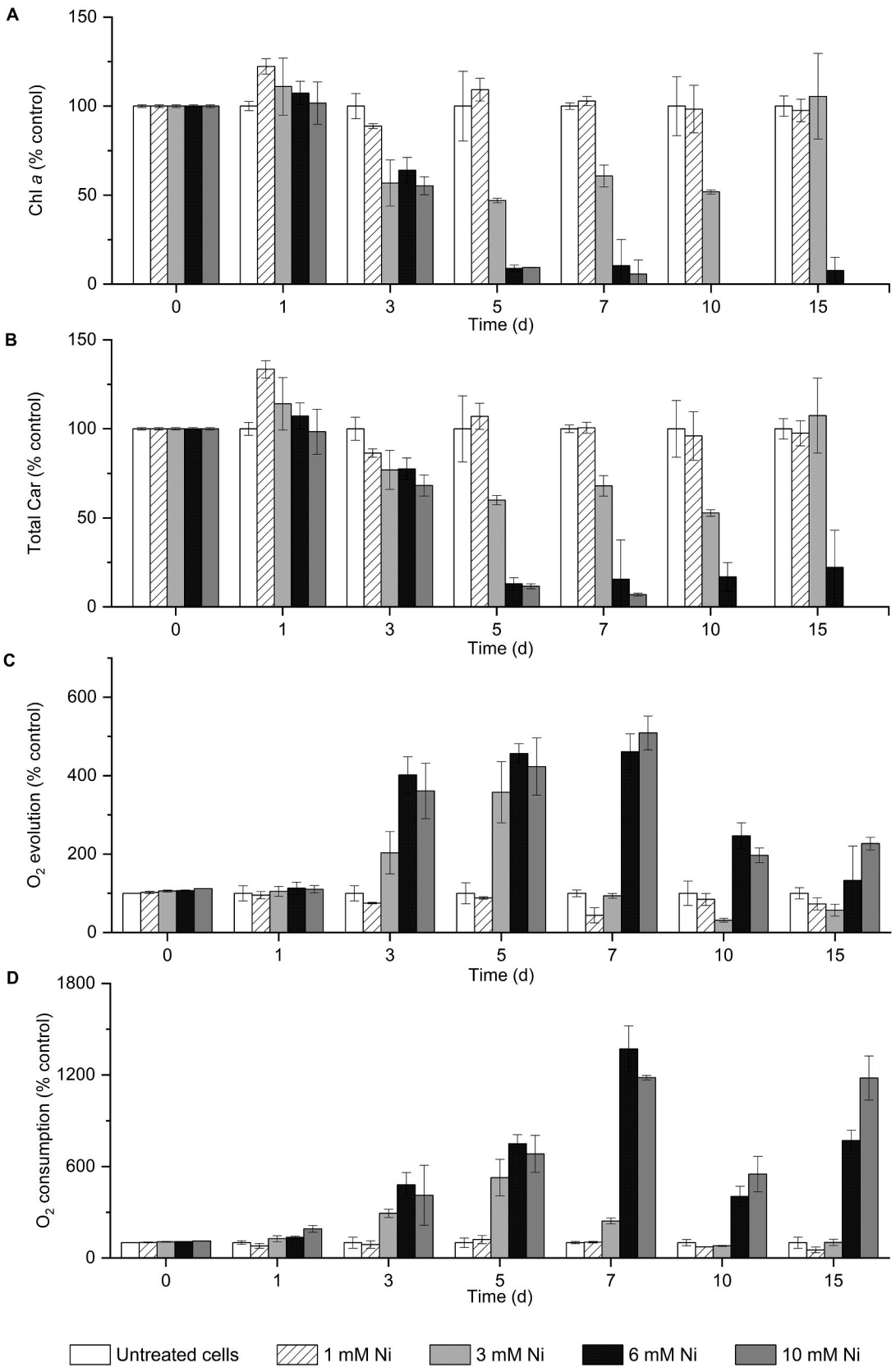

Fig. 2. Pigment quantification, oxygen evolution and consumption in *C. merolae* cells during long-term adaptation to various Ni concentrations. Shown are: quantification of chlorophyll *a* (A), total carotenoid content (B), oxygen evolution (C), and oxygen consumption (D). (A–B) The pigment content was expressed in pg of pigment per cell, and is normalized to the total pigment content of the control (% control, Chl *a* 0.0250–0.0485 pg cell^{-1} and total carotenoids 0.077–0.0141 pg cell^{-1}). (C–D) Oxygen values are expressed as nmoles of O_2 per 10^6 cells per hour, and normalized to the control (% control, O_2 evolution 0.78–2.07 nmol O_2 10^6 cells^{-1} h^{-1} and O_2 consumption 0.21–2.18 nmol O_2 10^6 cells^{-1} h^{-1}). Data is the mean ± SD of two independent biological replicas (n = 2).

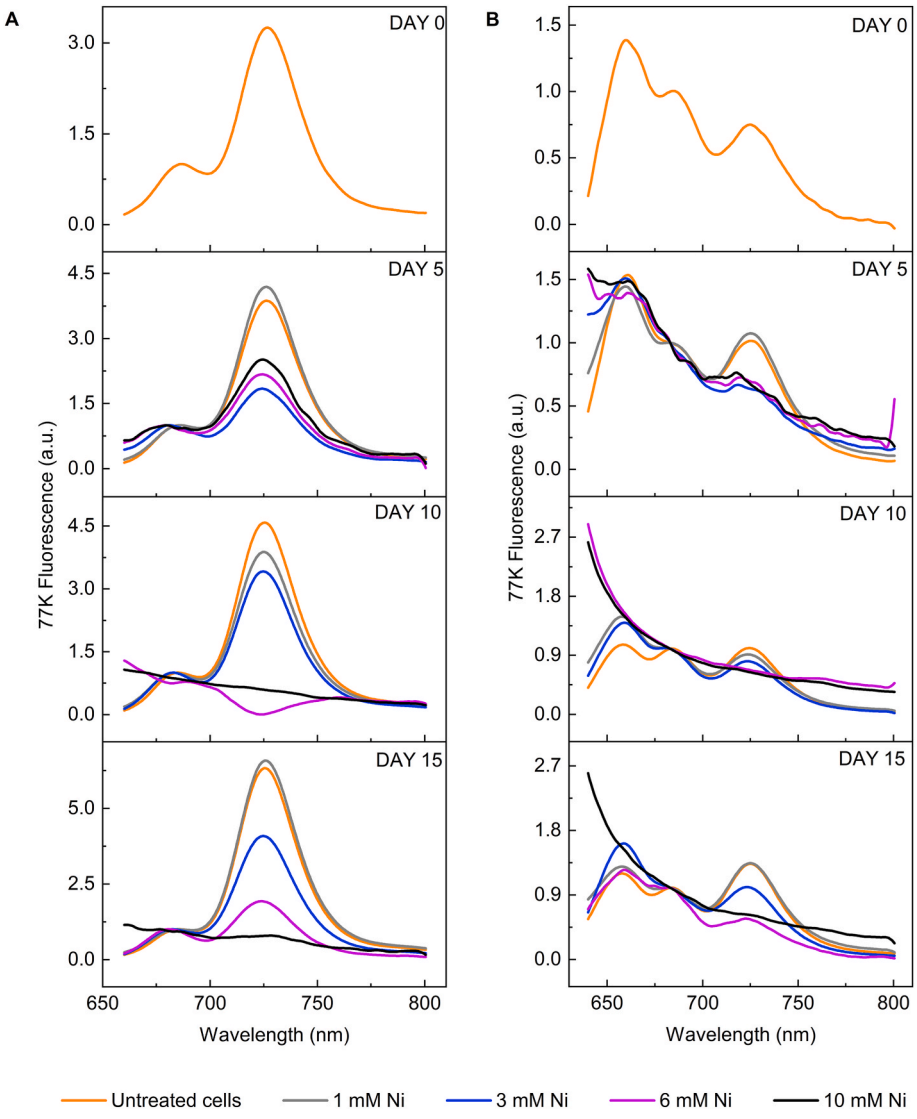

Fig. 3. 77K fluorescence spectroscopy of the *C. merolae* cells long-term adapted to various Ni concentrations. (A) corresponds to the emission spectra using Chl *a* excitation at 435 nm on days 5, 10 and 15, respectively. (B) corresponds to the emission spectra upon PBS excitation at 600 nm on days 5, 10 and 15, respectively. All spectra (2 μg Chl) were normalized to the PSII peak (685 nm) and were averaged from 2 biological replicas (n = 2).

Ankistrodesmus falcatus was inhibited by 90% (Santos et al., 2019) or 100% (Martínez-Ruiz and Martínez-Jerónimo, 2015) upon 15–45 μM Ni and 2 μM Ni exposure, respectively.

3.2. Functional resilience of the C. merolae photosynthetic apparatus upon high nickel exposure

In this study, we examined the functionality of the photosynthetic apparatus upon long-term exposure of *C. merolae* cells to high Ni, as photosynthesis provides the majority of metabolic energy required for maintenance of cellular homeostasis in this alga under adverse conditions such as heavy metal stress. It is well established that nickel is an essential micronutrient that is critical for sustaining cell growth. However, high concentrations of this metal negatively affect cell division in higher plants and most algae due to the inhibition of enzymatic activity including the components of the photosynthetic apparatus (Monteiro et al., 2012).

3.2.1. Pigment quantitative changes

The estimation of the total content of chlorophyll *a* (Chl *a*) and carotenoids (Car) in the *C. merolae* cells exposed to various Ni concentrations confirmed significant changes in the amount of both types of pigments during the treatment. On day 15 of 3 mM Ni exposure, the pigment content per cell was similar to the control (Fig. 2 A, B and Table S1). However, at 6 mM Ni, the total Chl *a* and Car content decreased by 92% and 78%, respectively, compared to the untreated cells, while at 10 mM Ni the values were beyond the detection threshold (Fig. 2A and B and Table S1). These observations are in line with the cell viability data (see Fig. 1C) which showed a significant decrease in the proportion of viable cells at 6 mM and 10 mM Ni. In higher plants, Ni treatment leads to dissociation of the entire photosynthetic complexes from the membranes or their specific subunits (Szalontai et al., 1999). Therefore, the decrease in the total photosynthetic and photoprotective pigment content observed here at the highest Ni concentrations is likely due to the degradation of the photosynthetic components. This is in contrast to other extremophilic microalgae, such as halophilic green alga *Dunaliella salina* in which an increase of the total Car content was observed during adaptation to elevated Fe levels (Mojaat et al., 2008).

The effect of Ni on the decrease in photosynthetic and photoprotective pigments is well documented when this heavy metal is used at much lower (μM) concentrations. For instance, in the green microalga *Ankistrodesmus falcatus* a decrease in the total Chl *a* and Car content after

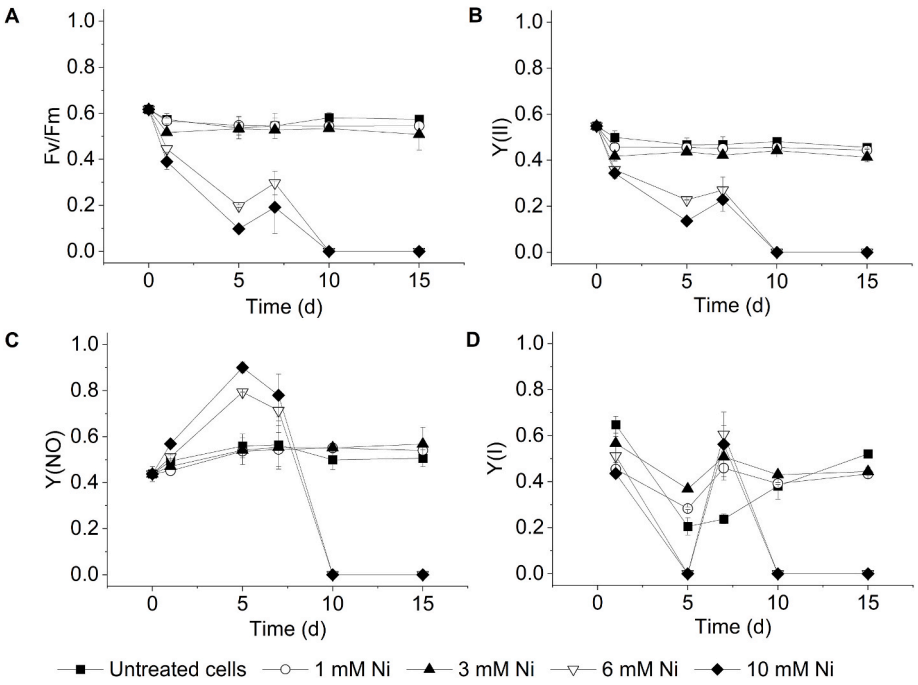

Fig. 4. DUAL-PAM analysis of photosynthetic performance in *C. merolae* cells long-term adapted to various nickel concentrations. Shown are: maximum efficiency of PSII (F_v/F_m ratio; A), effective photochemical efficiency of PSII (Y(II); B), non-regulated NPQ (Y(NO); C) and the effective photochemical efficiency of PSI (Y(I); D). Data for all parameters is the mean ± SD of two independent biological replicas (n = 2).

96 h treatment with 0.015–0.064 μM Ni was observed (Martínez-Ruiz and Martínez-Jerónimo, 2015). Similarly, three different *Spirulina* species exhibited a severe decrease in Chl content after exposure to 10–100 μM Ni (Balaji et al., 2014). Therefore, the pigment quantification data confirm the remarkable integrity of *C. merolae* photosynthetic machinery and photosynthetic membranes during adaptation to up to 3 mM Ni, in contrast to mesophilic microalgae and cyanobacteria.

3.2.2. *Steady-state 77K fluorescence analysis of C. merolae under nickel exposure*

The 77K Chl fluorescence analysis of the intact cells showed the relative changes in the functional antenna size of PSI (peaking at 726 nm) during long-term exposure of *C. merolae* to 1–10 mM Ni (Fig. 3A). On day 5, a 35–56% decrease in the antenna size of PSI was observed for the cells treated with 3, 6 and 10 mM Ni compared to the control and 1 mM Ni-treated cells. However, for 3 mM Ni-treated cells, the size of the PSI antenna seemed to recover to the control level on days 10 and 15. Similarly, PSI antenna recovery was observed for 6 mM Ni-treated cells (Fig. 3A). In the case of 10 mM Ni treatment, no PSII or PSI fluorescence was detected from day 5 until the end of the experiment. Upon excitation of the PBS, three main emission peaks were observed at 655 nm, 681 nm and 728 nm corresponding to phycocyanin, anchor polypeptide ApcE and PSI, respectively (Busch et al., 2010). An increase in the amplitude of the PBS emission was observed on day 10, for 1 and 3 mM Ni-treated cells, and on day 15 for 3 mM Ni (Fig. 3B and Table S2), which may indicate functional decoupling of PBS from PSII (Canonico et al., 2020) or increase in the overall PBS accumulation upon Ni treatment. The PSI peak is clearly identified in the emission spectra when PBS antennae are excited, confirming the maintenance of energy transfer between PBS and PSI at 1–3 mM Ni. The PSII peak was significantly blue-shifted in the case of the cells treated with 3–10 mM Ni (Table S3). A similar effect was observed in the case of conformational changes (Boussac et al., 2020) and/or subunit or pigment dissociation from the PBS/PSII complex (Andrizhiyevskaya et al., 2005), suggesting that a similar phenomenon may occur upon Ni treatment.

3.2.3. *Photosynthetic performance of C. merolae under nickel stress*

The presence of heavy metals including Ni inside the photosynthetic cells can directly affect the efficiency of the photosynthetic electron transfer at many levels including structural destabilization and catalytic inhibition of the donor side of PSII, e.g., by replacing Ca in the Mn_4O_5Ca cluster and extrinsic PsbO subunit, replacing Mg in the Chl molecules, or replacing haem and non-haem Fe (reviewed in Nowicka, 2022). Other effects of heavy metal treatment include aberration of the thylakoid membrane organization (e.g. membrane de-stacking), membrane lipid peroxidation leading to the formation of ROS species, oxidative damage of lipids, proteins and other biomolecules and direct inhibition of enzymes of the Calvin-Benson-Bassham cycle including RuBisCo and phosphoribulokinase (reviewed in Shahzad et al., 2018).

Of all the multi-level deleterious effects of heavy metals, it is important to assess the performance of the photosynthetic apparatus under this type of stress, especially in the context of the capability of the primary energy production during long-term adaptation to metal stress. One of the main and most important parameters that determine photosynthetic performance is the maximal quantum yield of PSII (F_v/F_m parameter), which corresponds to the maximum efficiency at which light absorbed by PSII is used for photochemistry (reduction of strongly bound quinone Q_A) (Baker, 2008).

As shown in Fig. 4A, F_v/F_m values of 0.57, 0.57 and 0.52 were obtained for the control, 1 and 3 mM Ni treated cells, respectively, confirming the presence of efficient photochemistry in PSII during cellular adaptation to up to 3 mM Ni. In contrast, at 6 and 10 mM Ni concentrations, an irreversible decrease of the F_v/F_m parameter was observed already after 24 h Ni exposure. The effective operating efficiency of PSII (Y(II)) parameter, (Fig. 4B) showed a similar trend, with values of 0.5 for the untreated cells, compared to 0.46 and 0.42 for 1 mM and 3 mM Ni-treated cells, respectively. This observation indicates that almost half of the absorbed quanta of light are effectively converted into photochemical energy in the PSII reaction centers during cellular adaptation to up to 3 mM Ni. As expected, the Y(II) parameter decreased to zero from day 10 for the 6 and 10 mM Ni treatment. This shutdown of the photosynthetic apparatus is clearly confirmed by the measurement of the Y(NO) (Fig. 4C) and Y(I) (Fig. 4D) parameters that correspond to non-regulated

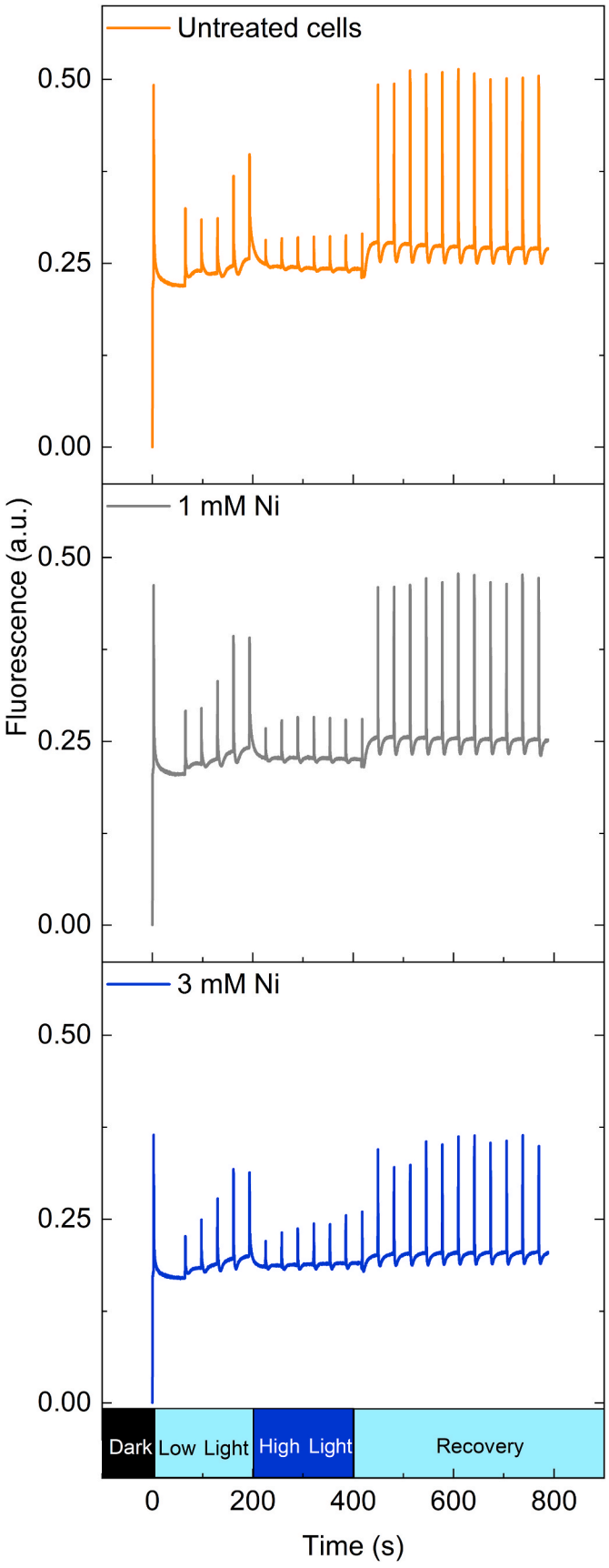

(caption on next column)

Fig. 5. Fluorescence induction kinetics analysis of the *C. merolae* cells exposed to Ni. After a long-term acclimation process (15 days), untreated cells, 1 mM Ni and 3 mM Ni treated cells were first dark adapted and then exposed to a sequence of different light pulses, as described in Materials and Methods. The 'Low Light' bar corresponds to a period of 200 s of low intensity blue light illumination (90 μE m^{-2} s^{-1}); 'High Light' bar corresponds to a period of 200 s of high intensity blue light illumination (1500 μE m^{-2} s^{-1}); while 'Recovery' bar corresponds to a 400 s period of low intensity blue light illumination (90 μE m^{-2} s^{-1}).

non-photochemical quenching (NPQ) (fraction of energy passively dissipated as heat and fluorescence) and effective quantum yield of PSI, respectively.

We then examined the efficiency of the regulated NPQ process which constitutes the fast photoprotective response triggered in PSII upon acidification of lumenal pH during exposure to various stressors including high light (Bassi and Dall'Osto, 2021; Krupnik et al., 2013) and heavy metals (Nowicka, 2022). The *in vivo* investigation of the NPQ kinetics (Fig. 5) during long-term adaptation of *C. merolae* cells to up to 3 mM Ni displayed the kinetic curves that were similar to the previously observed for cyanobacterial counterparts exposed to high light stress (Calzadilla and Kirilovsky, 2020). The exposure of dark-adapted cells to low intensity of blue light triggered a transient decrease in the maximum fluorescence of PSII (F_m'), which corresponds to the activation of NPQ response that was further enhanced during exposure to high intensity blue light followed by the full recovery of PSII fluorescence in the cells long-term adapted up to 3 mM Ni. These observations imply that the Ni-adapted cells are primed for the effective the NPQ response as the untreated counterparts (up to 3 mM Ni), in a process that is triggered even at low light intensities.

3.2.4. Analysis of oxygen evolution and consumption in C. merolae cells during Ni exposure

To further assess the functionality of the photosynthetic apparatus of *C. merolae* during long-term adaptation to high concentrations of Ni we performed the analysis of the oxygen evolution and consumption activities in the cell suspensions exposed to 1–10 mM Ni for up to 15 days. The overall oxygen evolution rate (net photosynthetic O_2 production) in *C. merolae* cells exposed to 6 and 10 mM Ni was significantly higher compared to the untreated samples (Fig. 2C) up to 7 days of Ni exposure followed by a rapid decrease of this parameter on days 10–15. This observation is in line with the PAM fluorescence data (Fig. 4). The molecular basis underlying the transient increase of O_2 production during adaptation to high Ni concentration is presently unknown. However, it is likely that the observed high oxygen evolution values are not physiologically significant taking in consideration the low number of cells present in the respective samples. Nevertheless, it is possible that the inhibition of the competing reactions, such as water-water cycle, light-induced mitochondrial respiration and/or photorespiration may be responsible for this phenomenon (Raven et al., 2020). An alternative explanation for the transient increase of O_2 evolution activity can represent an abiotic phenomenon, such as the formation of NiOx and NiFeOx species that may form at high Ni concentrations and have previously been shown to exhibit high water splitting activity (Garrido--Barros et al., 2019). All these intriguing possibilities will be addresses in the future studies.

We observed the highest net O_2 consumption rate (measure of mitochondrial respiration) on day 7 in the presence of 6 mM Ni (Fig. 2D). We hypothesized that the increase of this parameter could be due to the impairment or remodelling of the mitochondrial respiratory chain components upon Ni treatment. To shed light on this phenomenon, we applied 2,4-dinitrophenol (DNP) to the *C. merolae* cells adapted for 7 days to 3 and 6 mM Ni. DNP is a well-known mitochondrial protonophore that dissipates pH gradient across the mitochondrial membrane leading to uncoupling of oxidative phosphorylation from the mitochondrial electron transport chain (Goldgof et al., 2014). We

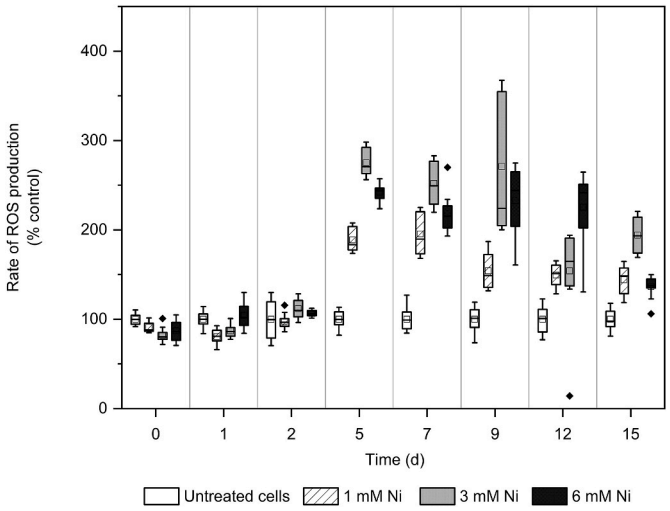

Fig. 6. Analysis of ROS production in *C. merolae* cells during long-term exposure to various nickel concentrations. The rate of ROS production was measured for each sample using the fluorescent probe, 2′,7′-dichlorodihydrofluorescein diacetate. Values correspond to the rates of ROS production normalized to protein concentration (μg mL^{-1}) and then expressed as a percentage of Ni untreated control (% control, 12.51–43.51 rate of ROS production per protein (μg mL^{-1}), that correspond to the minimum and maximum measured values during the 15 days experiment). The coloured boxes represent the interval data between 25 and 75% of the total values. The upper and lower whiskers correspond to the maximum and minimum values excluding the outliers. The black horizontal lines inside the boxes are the medians, while the squares are the average values and the rhombi correspond to the outlier values. Data is the mean ± SD of two independent biological replicas, with 6 technical replicas for each biological replica (n = 2).

hypothesized that if the respiratory chain components underwent the functional or structural impairment exerted by the intracellular Ni, the DNP treatment would not further increase their activity and thus, the overall oxygen consumption would be stable. However, the DNP treatment of Ni-adapted cells resulted in higher oxygen consumption rates in 3 mM Ni- and especially in 6 mM Ni-adapted cells (1.4 and 7.7 fold increase, respectively; Fig. S3). Such an increase is most likely due to hypothesized before remodelling and/or increase in the number of respiratory chain components. We therefore propose that increasing the amount of the respiratory chain molecular components serves as the efficient adaptive strategy of *C. merolae* cells that allows them to maintain the cellular energy homeostasis during long-term exposure to Ni. The verification of this intriguing hypothesis will be addressed in the future work.

3.2.5. ROS production in C. merolae cells long-term exposed to nickel

Elevated levels of heavy metals can induce generation of reactive oxygen species (ROS), e.g. superoxide, peroxide and singlet oxygen produced in the Haber–Weiss cycle, Fenton reactions and during the disruption of the photosynthetic electron chain. ROS cause cellular damage via depletion of enzyme activities, through lipid peroxidation, and reaction with nuclear proteins and DNA (Rezayian et al., 2019). In consequence, protein and lipid degradation occurs together with ion leakage, oxidative DNA damage, redox imbalance, and degradation of the cellular membranes, ultimately leading to programmed cell death (Nagajyoti et al., 2010). On the other hand, ROS may act as signalling molecules that induce the production of a network of antioxidants, antioxidant enzymes, and other stress-related molecules (Pinto et al., 2003).

The role of Ni in generation of ROS-induced oxidative stress in plant and algal cells is related mainly to chromosome aberrations, disturbed structure of the chloroplast and competition or replacement of other metal cations such as Mg^{2+} in Chl molecules and Calvin cycle enzymes, or Ca^{2+} in the oxygen evolving complex of PSII (reviewed in Nowicka, 2022). We therefore examined the Ni-induced adaptability of *C. merolae* to ameliorate the cellular ROS levels by measuring the rates of ROS production at different timepoints of Ni adaptation and expressing those relative to the ROS production rates in the untreated cells (Fig. 6). We observed the significantly highest increase of ROS production rate on day 5 for all the Ni treatments ($p < 0.01$). This data confirms that during long-term adaptation of *C. merolae* to high Ni concentration, the ROS level is inherently high, even in the first days of cellular adaptation to 1 and 3 mM Ni when the cell growth and viability are similar compared to the control (Fig. 1A and C). Despite the generally higher levels of ROS in Ni-adapted cells compared to the non-stressed cells, the ROS amelioration metabolic machinery is capable of reducing their levels, as shown by the sinusoidal character of the ROS production curves. We therefore propose that the ROS amelioration pathways are likely to be highly active in *C. merolae* cells during long-term high Ni adaptation. Global transcriptomic and proteomic analyses are underway to confirm this hypothesis.

3.2.6. Association of nickel with C. merolae cells

At the cellular level, the defence mechanisms to a metal ion can be either exclusion of the metal from the cell, the uptake and modification of the metal to a less toxic form, followed by the metal extrusion from the cell, or internal sequestration (Hall and Williams, 2003). A common strategy for heavy metal detoxification is metal compartmentalization and sequestration in different cellular organelles such as vacuoles or as electron dense bodies in the cytosol, chloroplasts and mitochondria (Sharma et al., 2016). In various microalgal species, the vacuole is the main locus for sequestration of metals. Thus, in *Pseudochlorococcum typicum* the exposure of cells to Pb caused the formation of spherical electron-dense bodies in the vacuole (Shanab et al., 2012). On the other hand, *C. reinhardtii* and *E. gracilis* microalgae sequester Cd complexes in the chloroplast and, in the case of *E. gracilis* additionally in the mitochondrion (Hanikenne et al., 2009; Mendoza-Cózatl and Moreno-Sánchez, 2005). The absence of typical vacuoles in *C. merolae* combined with its remarkable adaptability to high concentrations of Ni (as shown by this study) implies that this alga may have evolved efficient mechanisms of detoxification of this heavy metal. Interestingly, *C. caldarium,* another member of Cyanidiales that contains large vacuoles, has been shown to deposit high levels of metals such as Fe, Al and Zn in cytoplasmic electron dense bodies (Nagasaka et al., 2004).

In the case of *C. merolae*, no data has been reported to date on the exact localization of Ni within the cellular compartments or its putative association with the cell membrane during long-term adaptation to this

Table 1
Nickel quantification by ICP-MS in *C. merolae* cells long-term adapted to various Ni concentrations. Quantification of Ni is shown for the growth medium (supernatant; mg Ni L^{-1}) and the lysate (mg Ni g^{-1} of wet biomass). Data corresponds to the mean ± SD of two independent biological replicas (n = 2).

Time (day)	Untreated cells		1 mM Ni		3 mM Ni	
	Supernatant (mg L^{-1})	Lysate (mg g^{-1})	Supernatant (mg L^{-1})	Lysate (mg g^{-1})	Supernatant (mg L^{-1})	Lysate (mg g^{-1})
0.25	$4.04{\cdot}10^{-3} \pm 0.013{\cdot}10^{-1}$	$4.39{\cdot}10^{-5} \pm 0.008{\cdot}10^{-3}$	55.89 ± 1.7	0.02 ± 0.001	184.71 ± 4.56	0.57 ± 0.12
5	$4.22{\cdot}10^{-3} \pm 0.014{\cdot}10^{-1}$	$8.74{\cdot}10^{-5} \pm 0.009{\cdot}10^{-3}$	58.30 ± 0.58	0.03 ± 0.002	193.09 ± 14.37	0.10 ± 0.02
10	$4.30{\cdot}10^{-3} \pm 0.017{\cdot}10^{-1}$	$1.28{\cdot}10^{-5} \pm 0.002{\cdot}10^{-2}$	60.97 ± 1.21	$0.01 \pm 0.007{\cdot}10^{-1}$	214.62 ± 13.82	0.08 ± 0.02
15	$3.69{\cdot}10^{-3} \pm 0.056{\cdot}10^{-2}$	$4.16{\cdot}10^{-5} \pm 0.017{\cdot}10^{-3}$	66.24 ± 0.51	$0.01 \pm 0.006{\cdot}10^{-1}$	197.74 ± 10.37	0.07 ± 0.02

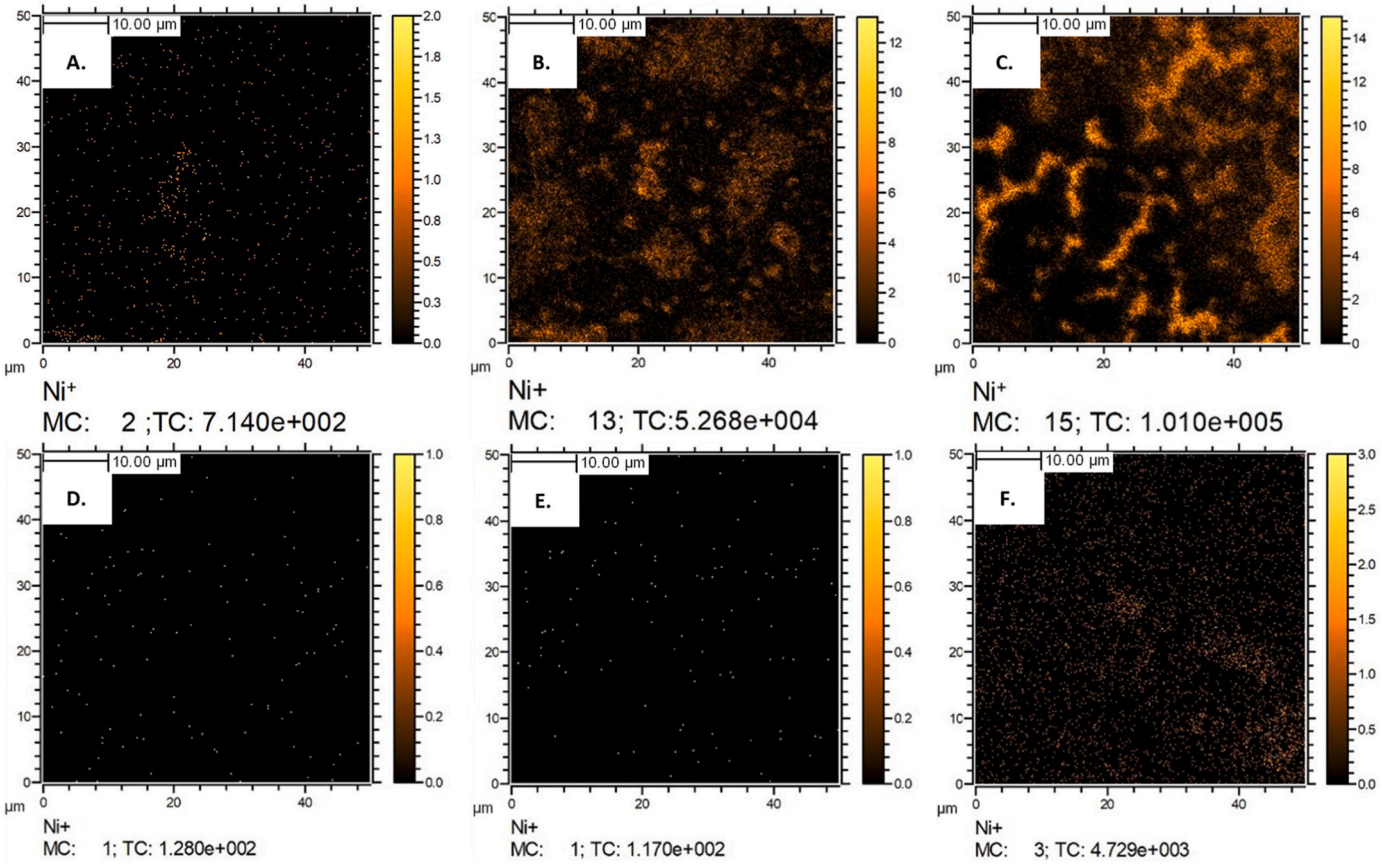

Fig. 7. Nickel ion mapping of the *C. merolae* cells using Time-of-Flight Secondary Ion Mass Spectrometry. Micrographs correspond to a 10 µm × 10 µm area of immobilized *C. merolae* cells exposed to varying concentration of Ni. A-C, Ni maps of the samples without any processing; D-F, Ni maps of the samples subjected to the one-step washing. The concentration of Ni^{2+} in the growth medium was 1 mM (A, D), 3 mM (B, E), and 6 mM (C, F). The colour scale bar on the right of each figure shows the number of Ni ion counts collected at the corresponding point. Scale bar: 10 µm. MC – maximum number of counts per pixel (also shown as a scale), TC - total number of counts. The small white spots correspond to random spike noise signal.

heavy metal. To gain insight into this issue, a combined electron microscopy and elemental analysis was performed on *C. merolae* cells long-term exposed to various concentrations of Ni at different time points using three independent approaches. The elemental analysis based on Inductively Coupled Plasma Mass Spectrometry (ICP-MS) showed that for all the Ni concentrations applied less than 1% of the total Ni added to the growth medium is associated with the cells (Table 1). As expected, the amount of Ni present in the cell lysate at 3 mM Ni is more than 3-fold higher compared to the samples exposed to 1 mM Ni for all the time points except for day 5 samples (2.8-fold increase, Table 1). The level of Ni present in the lysate of 1 mM Ni treated cells is constantly low at different timepoints (0.01–0.03 mg/g), demonstrating that the cells were able to efficiently adapt to this concentration of metal throughout the treatment despite the cyclic increase of the cellular ROS level (Fig. 6).

In an independent approach based on Time-of-Flight Secondary Ion Mass Spectrometry (TOF-SIMS) we confirmed that the majority of Ni is loosely associated with the *C. merolae* cell membrane. SIMS is a destructive method of analysis. Due to the interactions with the environment (matrix effect) and the higher probability of emission, the above mentioned metal ions are predominantly the single charged particles (Benninghoven, 1994). Therefore, the obtained Ni^{+} distribution maps can be equated with the occurrence signal from the Ni associated either with *C. merolae* cells and/or with Ni deposited during evaporation of growth medium.

Fig. 7 presents the Ni^{+} ion emission SIMS-TOF maps registered for the *C. merolae* cells immobilized on the silicon substrate following their 15-day exposure to 1–6 mM Ni. The maps presented in the upper row (Fig. 7A–C) correspond to the samples without any washing processing (see Materials and Methods, section 4). Upon increasing Ni^{2+} concentration in the bulk of solution the increase in the amount of Ni deposited on the cells is clearly visible. In contrast, no significant Ni signal was observed for the cells subjected to the washing procedure (Fig. 7D–F). In the latter case, the signal is much weaker indicating that most of Ni visible in Fig. 7A–C was physically adsorbed on the cell surface. The low intensity of the observed signal may be explained by nature of the SIMS-TOF technique. The sampling depth of this technique is approximately 1–3 nm (Muramoto et al., 2012), thus the ion maps represent the signal collected from the cell surface.

The SIMS spectra were analysed for the signals from the substrate (Si^{+}) and from the algal cells (Fig. S4). The organic fragment, $C_3H_8N^{+}$, was chosen as representative SIMS marker for the organic matter of the cells as it corresponds to the product of peptide ionization (Schönwälder et al., 2014; Thiruvallur Eachambadi et al., 2021) and its mass is close to the mass of the main isotope of Ni. The Ni content for low-concentration (1 and 3 mM Ni) cultures correlates with the presence of the organic ion (Figs. S5 and S6) indicating the adsorption of this ion on the cell surface. However, for the 6 mM Ni-treated samples some differences were observed. Spots of the local Ni accumulation, which do not correlate with the presence of organic structures, were detected (Figs. S5 and S6). This may indicate that a significant portion of Ni remains in the solution in the ionic form. The association of Ni with the cell membrane was also confirmed by the analysis based on Scanning Electron Microscopy combined with Energy Dispersive X-Ray Spectroscopy (SEM-EDS), whereby the majority of Ni is detected on the cell surface (Fig. 8).

The low intracellular level of Ni in *C. merolae* cells observed in our

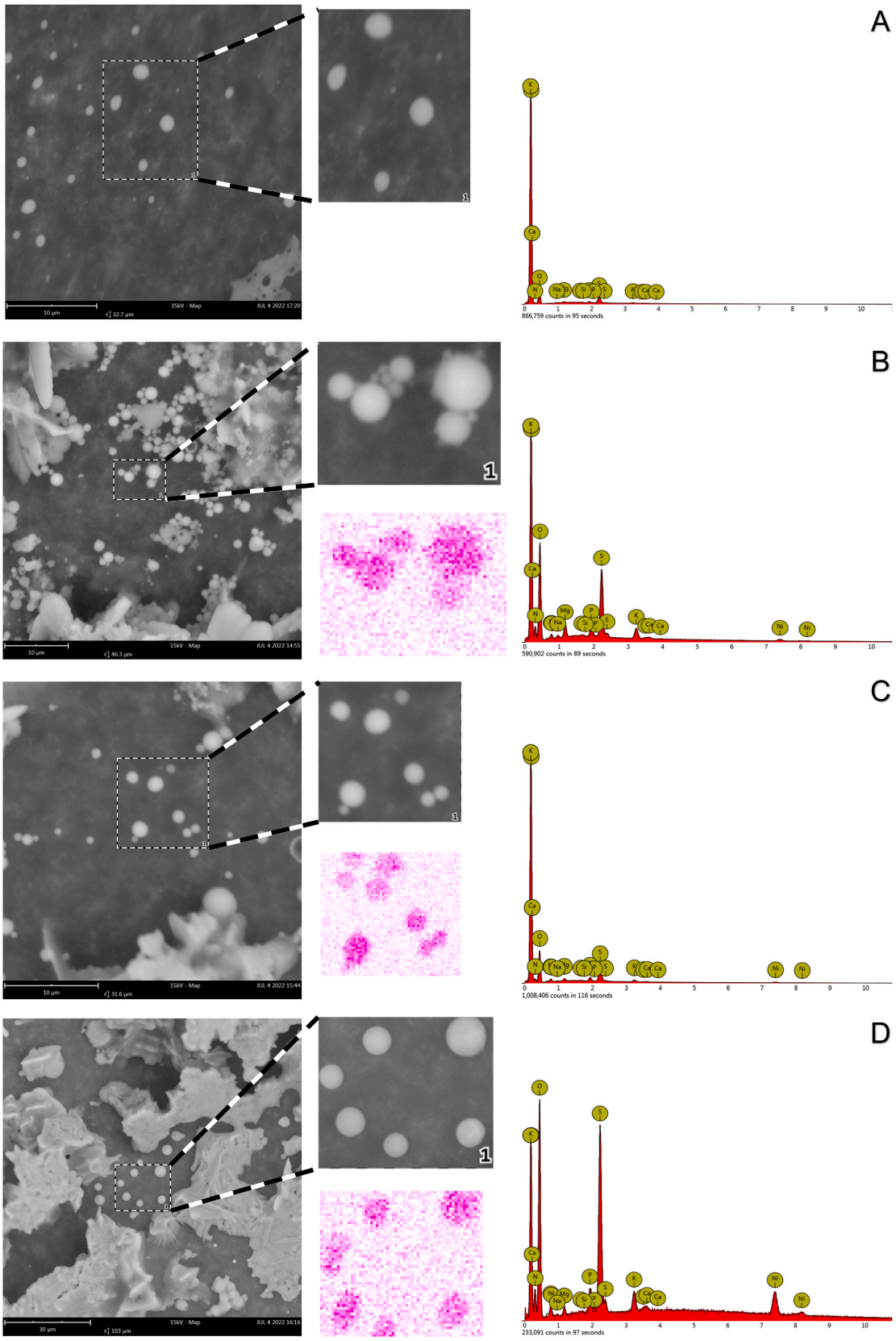

Fig. 8. SEM-EDS imaging of Ni in *C. merolae* cells long-term adapted to various nickel concentrations. Each panel corresponds to a different treatment (day 5 of Ni exposure), either (A) untreated cells; (B) 1 mM Ni; (C) 3 mM Ni; and (D) 6 mM Ni treated cells. For each panel shown is: micrograph with the scale bar (left), the magnified spot of selected cells to be analysed, the EDS micrograph of Ni (center); and the spectra of the EDS map (right). Scale bars: 10 μm (A, B, C) and 30 μm in (D).

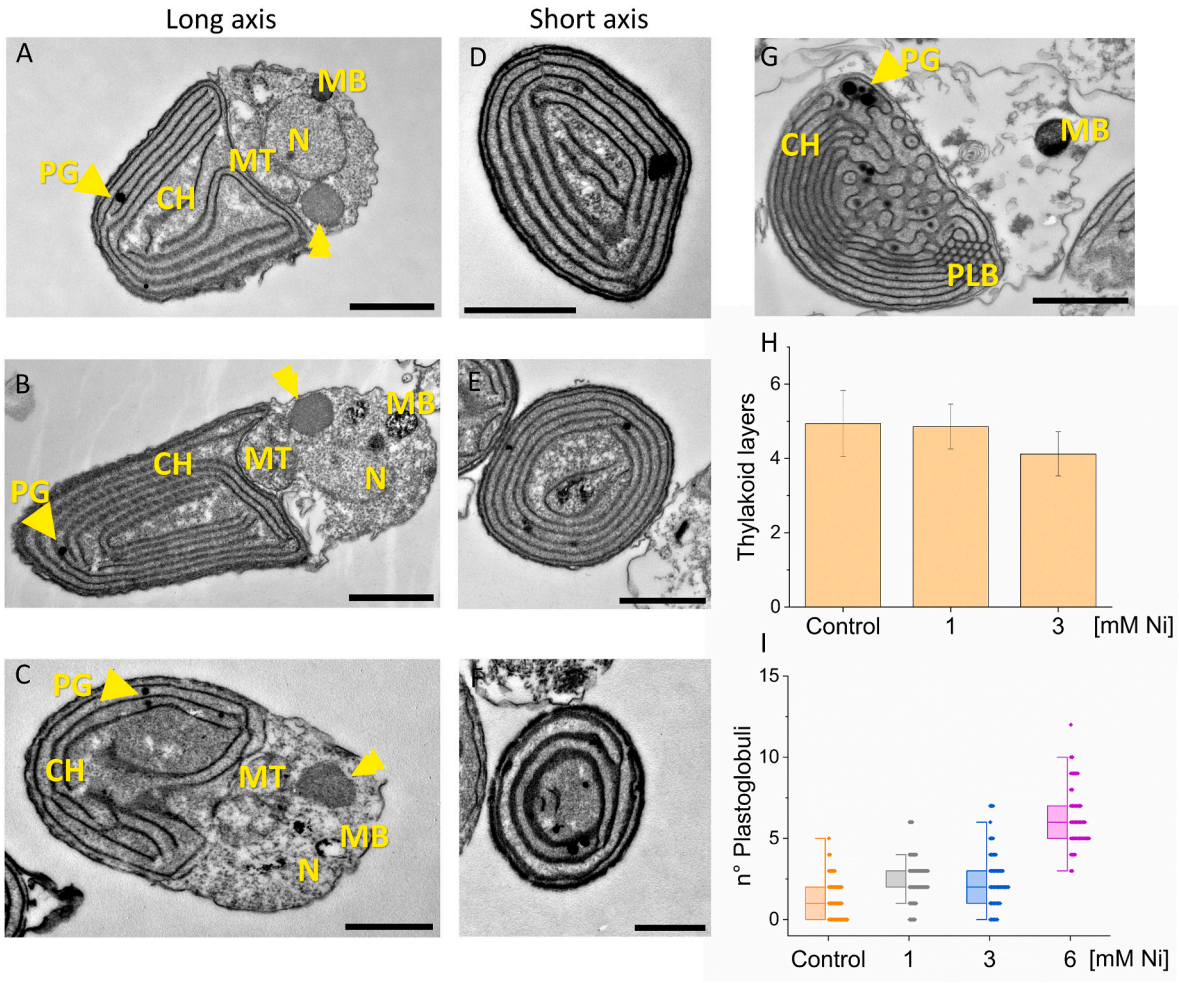

Fig. 9. TEM imaging of *C. merolae* cells during long-term adaptation to various nickel concentrations. (A, D), untreated cells; (B, E), cells exposed to 1 mM Ni; (C, F), cells exposed to 3 mM Ni; and (G), cells exposed to 6 mM Ni for 7 days. For each Ni treatment, cells are visualized along the long (A, B, C) and short axes (D, E, F). (H): Quantification of the number of thylakoids on day 7 of the experiment. (I): Quantification of the number of plastoglobules in the chloroplasts of the cells after 7 days of treatment. Data corresponds to the mean ± SD following the analysis of 50 cells (per each sample) using two independent biological replicas (n = 2). N: nucleus, CH: chloroplast, MT: mitochondrion, PG: plastoglobules, PLB: prolamellar body, MB: microbody, arrowhead depicts a vacuole-like organelle. Scale bar: 1 μM.

study is likely due to basal active extrusion of this heavy metal or other mechanisms that prevent the Ni accumulation inside the cells, thus protecting the cellular metabolism from the deleterious effect of high Ni levels. It is unlikely that the cells do not uptake Ni, e.g., by passive diffusion, taking into account large amount of this heavy metal in the external environment. The postulate of active Ni extrusion is supported by the physiological data showing no significant differences in the growth curves or photosynthetic parameters at 1 mM Ni compared to the untreated cells (Fig. 1A and Fig. 4). In contrast, the Ni content in the cell lysate at 3 mM Ni decreases progressively during 15-day treatment from 0.57 mg/g in the first 6 h to 0.10 mg/g and 0.07 mg/g on days 5 and 15 of the treatment, respectively (Table 1). We propose that metabolic fine-tuning occurred during the first 5 days of the Ni treatment that promoted inducible active Ni extrusion and additional Ni defence mechanisms (over and above the basal Ni active extrusion). This hypothesis is in line with the physiological data of partial inhibition of cell growth at 3 mM Ni within the same timeframe followed by the recovery phase (Fig. 1A). In the case of 6 and 10 mM Ni, due to severe inhibition in the cell growth (Fig. 1A) and low cell viability (Fig. 1C) the elemental analysis on these samples was not possible. Interestingly, in the *C. merolae* genome several molecular components have been identified that can be involved in the active Ni extrusion from the cells including different zinc transporters or mitochondrial ABC transporters (Hanikenne et al., 2005). Transcriptomic and proteomic analyses are currently underway to identify the specific molecular components in *C. merolae* involved in the putative active Ni efflux.

3.2.7. Structural changes to thylakoid organization during C. merolae adaptation to high nickel concentration

Exposure to toxic metal ions may affect substantial changes to thylakoid membrane organization as shown for another member of Cyanidiales, the red alga *C. caldarium* exposed to Al (Nagasaka et al., 2002). These changes may occur at different levels including alteration of the membrane integrity through lipid peroxidation, degradation of protein components embedded within thylakoids and alteration of the ionic milieu affecting the dynamics of membrane stacking and unstacking (Nowicka, 2022). *C. merolae* has a simple cellular ultrastructure, with up to $^{2}/_{3}$ of the cell volume occupied by a single chloroplast under non-stress conditions. In this microalga, thylakoids do not form grana or stromal lamellae but are organized into a network of loosely positioned membranes (Miyagishima and Tanaka, 2021).

To observe the putative changes of the thylakoid architecture during long-term adaptation of *C. merolae* to the Ni stress we performed, after 7 days of exposure, Transmission Electron Microscopy (TEM) analysis of the cellular ultrastructure of 1–6 mM Ni-treated cells (Fig. 9 and Fig. S7). We observed no significant differences in the number of thylakoids or

their spatial organization in the 1 mM Ni samples compared to the untreated control (Fig. 9A/D and 9B/E). However, during adaptation of *C. merolae* cells to Ni concentrations above 1 mM, significant structural changes were observed in the chloroplasts. In 3 mM Ni-treated cells, the number of thylakoids was significantly lower compared to the control and 1 mM Ni-treated cells (Fig. 9C–F and H), despite high cell viability (Fig. 1C) and high photosynthetic activity (Fig. 4) at this Ni concentration. At 6 mM Ni, it was not possible to calculate the number of thylakoids due to the strong aberration of the chloroplast structure. Not only were the number of thylakoid layers but also the chloroplast size affected by exposure to 3 and 6 mM Ni. The cells adapted to 1 and 3 mM Ni showed a slightly shorter longitudinal axis compared to the control sample (2.32 *versus* 2.14 and 2.15 μm for untreated cells and cells exposed to 1 and 3 mM Ni, respectively) after 15 days of metal exposure ($p < 0.01$), as estimated by confocal fluorescence imaging (see Fig. 1C). In the case of 6 and 10 mM Ni it was not possible to estimate the chloroplast size after 15 days of experiment due to the low viability and their susceptibility to rupture.

The characteristic feature of the chloroplasts exposed to 6 mM Ni was the presence of tubular prolamellar body (PLB)-like structures (Fig. 9G). The PLBs constitute the lipid reservoirs for developing thylakoids and have been shown to prevent lipid peroxidation and RNA damage under oxidative stress conditions (Solymosi and Mysliwa-Kurdziel, 2021). The PLBs have been observed in association with both cyanobacterial thylakoids and eukaryotic chloroplasts and represent a unique non-lamellar, but cubic-phase inner membrane structures. In spite of the similar lipid composition, major differences are observed in the protein composition of chloroplast thylakoids and PLBs (reviewed Solymosi and Mysliwa-Kurdziel, 2021) with the latter containing much higher lipid: protein ratio and high content of the light-dependent NADPH:protochlorophyllide oxidoreductase (LPOR), and enzyme catalysing protochlorophyllide photoreduction. The lipid-dependent formation of the photoactive LPOR oligomers was proposed to be a mechanism inducing the formation of the PLBs (Gabruk et al., 2017). We therefore postulate that the formation of PLBs in the *C. merolae* chloroplasts subjected to 6 mM Ni stress may constitute the adaptive mechanism triggered in response to high Ni stress required for the repair of the photosynthetic components.

Another structural feature observed in this study for Ni-adapted chloroplasts is an increased number of plastoglobuli (PGs) which are lipoprotein structures participating in chloroplast metabolism and stress responses (Arzac et al., 2022). On average, the number of PGs in the chloroplasts of the cells adapted to 1 mM and 3 mM Ni increased 2-fold compared to the control after 7 days of Ni exposure (Fig. 9I). In the chloroplasts adapted to 6 mM Ni, the increase was 6-fold compared to the control. For 10 mM Ni it was not possible to count the number of PGs due to the low cell viability impaired intactness at such high metal concentration.

It is well documented that the quantity and size of PGs increase in response to many types of biotic and abiotic stresses (reviewed in Venzhik et al., 2019) as for example heavy metal toxicity (El-Banna et al., 2019), temperature stress (Zhang et al., 2010), and pathogens (Raman et al., 2006). Such active involvement of PGs in various stress adaptation processes is underpinned by their diverse functional and metabolic roles (Arzac et al., 2022; Lundquist et al., 2012). Therefore, the increase of the number of PGs observed in this study is in line with the active metabolic role of these stress-marker organelles during *C. merolae* adaptation to high concentrations of Ni.

4. Conclusions

In this work, we have performed comprehensive analysis of the long-term adaptive responses of cells of a thermo-acidophilic microalga *C. merolae* to extremely high Ni levels (applied in the mM range). The complementary spectroscopic, microscopic and elemental analyses allowed us to dissect several mechanisms underlying the long-term adaptation to high Ni concentration. These include: (*i*) lack of significant Ni accumulation inside the cells as demonstrated by the complementary microscopic and elemental SIMS, SEM-EDS and ICP-MS analyses likely due to active Ni extrusion or by blocking the influx of the metal into the cell; (*ii*) maintaining the efficient photoprotective responses including NPQ (up to 3 mM Ni) primed by the Ni exposure; (*iii*) dynamic remodelling of the chloroplast ultrastructure such as formation of metabolically active PLBs and PGs together with loosening of the thylakoid membrane architecture as shown by TEM analysis; (*iv*) ROS amelioration as demonstrated by the dynamic regulation of ROS production and maintenance of relatively high cell viability up to 3 mM Ni; and (*v*) sustaining the efficient respiratory chain functionality likely by increasing the amount of the respiratory chain components as demonstrated by the marked stimulation of oxygen consumption in response to pharmacological uncoupling of the mitochondrial membranes. All the dynamic processes identified in our study underlie the capability of *C. merolae* to adapt efficiently to extremely high Ni levels that exceed by several orders of magnitude the levels of this heavy metal in the natural environment of this extremophilic microalga. Our study paves the way for the biotechnological application of this extremophile in heavy metal recycling and metabolic engineering of new traits in higher plants and microalgae for high heavy metal tolerance/sequestration.

Funding

This work was supported by the National Science Centre of Poland [OPUS 17 grant no. 2019/33/B/NZ3/01870 to J.K. and MINIATURA 5 grant no. 2021/05/X/NZ2/01516 to S.S.]; Transmission Electron Microscopy (TEM) experiments were performed at the Nencki Institute, PAS, using infrastructure of the Polish Euro-BioImaging Node. Part of the TEM work was supported by the Ministry of Education and Science [No. 2022/WK/05, Polish Euro-BioImaging Node "Advanced Light Microscopy Node Poland"].

CRediT authorship contribution statement

Francesca Marchetto: Formal analysis, Investigation, Methodology, Writing – original draft, Writing – review & editing, Validation, Visualization. **Sergio Santaeufemia:** Formal analysis, Investigation, Methodology, Writing – original draft, Funding acquisition. **Magdalena Lebiedzińska-Arciszewska:** Formal analysis, Methodology, Validation, Writing – review & editing. **Małgorzata A. Śliwińska:** Formal analysis, Investigation, Methodology, Visualization, Writing – review & editing. **Magdalena Pich:** Formal analysis, Methodology. **Eliza Kurek:** Formal analysis, Methodology. **Aleksandra Naziębło:** Formal analysis, Methodology. **Marcin Strawski:** Formal analysis, Investigation, Methodology, Validation, Visualization, Writing – original draft, Writing – review & editing. **Daniel Solymosi:** Methodology, Validation, Writing – review & editing. **Marek Szklarczyk:** Formal analysis, Methodology, Validation, Writing – review & editing. **Ewa Bulska:** Formal analysis, Methodology, Validation. **Jędrzej Szymański:** Funding acquisition, Methodology, Validation, Visualization, Writing – review & editing. **Małgorzata Wierzbicka:** Formal analysis, Methodology, Validation, Writing – review & editing. **Yagut Allahverdiyeva:** Methodology, Validation, Writing – review & editing. **Mariusz R. Więckowski:** Formal analysis, Methodology, Validation, Writing – review & editing. **Joanna Kargul:** Conceptualization, Data curation, Formal analysis, Funding acquisition, Methodology, Project administration, Resources, Supervision, Validation, Writing – original draft, Writing – review & editing.

Declaration of competing interest

The authors declare that they have no known competing financial interests or personal relationships that could have appeared to influence the work reported in this paper.

Data availability

The data underlying this article will be shared on reasonable request to the corresponding author (JK).

Appendix A. Supplementary data

Supplementary data to this article can be found online at https://doi.org/10.1016/j.plaphy.2024.108365.

References

Allen, M.B., 1959. Studies with *Cyanidium caldarium*, an anomalously pigmented chlorophyte. Arch. Mikrobiol. 32, 270–277. https://doi.org/10.1007/BF00409348.

Andrizhiyevskaya, E.G., Chojnicka, A., Bautista, J.A., Diner, B.A., van Grondelle, R., Dekker, J.P., 2005. Origin of the F685 and F695 fluorescence in photosystem II. Photosynth. Res. 84, 173–180. https://doi.org/10.1007/s11120-005-0478-7.

Arzac, M.I., Fernández-Marín, B., García-Plazaola, J.I., 2022. More than just lipid balls: quantitative analysis of plastoglobule attributes and their stress-related responses. Planta 255, 62. https://doi.org/10.1007/s00425-022-03848-9.

Baker, N.R., 2008. Chlorophyll fluorescence: a probe of photosynthesis in vivo. Annu. Rev. Plant Biol. 59, 89–113. https://doi.org/10.1146/annurev.arplant.59.032607.092759.

Balaji, S., Kalaivani, T., Rajasekaran, C., 2014. Biosorption of Zinc and Nickel and its effect on growth of different *Spirulina* strains. Clean: Soil, Air, Water 42, 507–512. https://doi.org/10.1002/clen.201200340.

Bassi, R., Dall'Osto, L., 2021. Dissipation of light energy absorbed in excess: the molecular mechanisms. Annu. Rev. Plant Biol. 72, 47–76. https://doi.org/10.1146/annurev-arplant-071720-015522.

Benninghoven, A., 1994. Chemical analysis of inorganic and organic surfaces and thin films by static time-of-flight secondary ion mass spectrometry (TOF-SIMS). Angew. Chem., Int. Ed. Engl. 33, 1023–1043. https://doi.org/10.1002/anie.199410231.

Borella, L., Vesce, L., Mariani, P., Barichello, J., Di Carlo, A., Trivellin, N., Sforza, E., 2022. Spectral changes by dye sensitized solar modules influence the pigment composition and productivity of *Arthrospira maxima* and increase the overall energy efficiency. Adv. Sustain. Syst. 6, 2100346 https://doi.org/10.1002/adsu.202100346.

Boussac, A., Sellés, J., Sugiura, M., 2020. What can we still learn from the electrochromic band-shifts in Photosystem II? Biochim. Biophys. Acta Bioenerg. 1861, 148176 https://doi.org/10.1016/j.bbabio.2020.148176.

Bradford, M.M., 1976. A rapid and sensitive method for the quantitation of microgram quantities of protein utilizing the principle of protein-dye binding. Anal. Biochem. 72, 248–254. https://doi.org/10.1016/0003-2697(76)90527-3.

Busch, A., Nield, J., Hippler, M., 2010. The composition and structure of photosystem I-associated antenna from *Cyanidioschyzon merolae*. Plant J. 62, 886–897. https://doi.org/10.1111/j.1365-313X.2010.04202.x.

Calzadilla, P.I., Kirilovsky, D., 2020. Revisiting cyanobacterial state transitions. Photochem. Photobiol. Sci. 19, 585–603. https://doi.org/10.1039/C9PP00451C.

Canonico, M., Konert, G., Kaňa, R., 2020. Plasticity of cyanobacterial thylakoid microdomains under variable light conditions. Front. Plant Sci. 11, 586543 https://doi.org/10.3389/fpls.2020.586543.

Carr, G.M., Neary, J.P., 2008. Water Quality for Ecosystem and Human Health. UNEP/Earthprint. https://wedocs.unep.org/xmlui/handle/20.500.11822/12217 (visited 15/02/2023).

Eisler, R., 1998. Nickel Hazards to Fish, Wildlife, and Invertebrates: A Synoptic Review. U.S. Department of the Interior, U.S. Geological Survey, Patuxent Wildlife Research Center. Report 34 ; Biological Science Report USGS/BRD/BSR–1998-0001.

El-Banna, M.F., Mosa, A., Gao, B., Yin, X., Wang, H., Ahmad, Z., 2019. Scavenging effect of oxidized biochar against the phytotoxicity of lead ions on hydroponically grown chicory: an anatomical and ultrastructural investigation. Ecotoxicol. Environ. Saf. 170, 363–374. https://doi.org/10.1016/j.ecoenv.2018.12.011.

Gabruk, M., Mysliwa-Kurdziel, B., Kruk, J., 2017. MGDG, PG and SQDG regulate the activity of light-dependent protochlorophyllide oxidoreductase. Biochem. J. 474, 1307–1320. https://doi.org/10.1042/BCJ20170047.

Garrido-Barros, P., Grau, S., Drouet, S., Benet-Buchholz, J., Gimbert-Suriñach, C., Llobet, A., 2019. Can Ni Ni complexes behave as molecular water oxidation catalysts? ACS Catal. 9, 3936–3945. https://doi.org/10.1021/acscatal.8b03953.

Goldgof, M., Xiao, C., Chanturiya, T., Jou, W., Gavrilova, O., Reitman, M.L., 2014. The chemical uncoupler 2,4-dinitrophenol (DNP) protects against diet-induced obesity and improves energy homeostasis in mice at thermoneutrality. J. Biol. Chem. 289, 19341–19350. https://doi.org/10.1074/jbc.M114.568204.

Hall, J.L., Williams, L.E., 2003. Transition metal transporters in plants. J. Exp. Bot. 54, 2601–2613. https://doi.org/10.1093/jxb/erg303.

Hanikenne, M., Krämer, U., Demoulin, V., Baurain, D., 2005. A comparative inventory of metal transporters in the green alga *Chlamydomonas reinhardtii* and the red alga *Cyanidioschizon merolae*. Plant Physiol. 137, 428–446. https://doi.org/10.1104/pp.104.054189.

Hanikenne, M., Merchant, S.S., Hamel, P., 2009. Chapter 10 - transition metal nutrition: a balance between deficiency and toxicity. In: Harris, E.H., Stern, D.B., Witman, G.B. (Eds.), The *Chlamydomonas* Sourcebook, second ed. Academic Press, London, pp. 333–399. https://doi.org/10.1016/B978-0-12-370873-1.00018-6.

Harris, E.H., 1989. The *Chlamydomonas* Sourcebook: a Comprehensive Guide to Biology and Laboratory Use. Academic Press, San Diego, p. 780. https://doi.org/10.1111/j.1469-8137.2009.03148.x.

Hirschberg, J., Chamovitz, D., 1994. Carotenoids in *cyanobacteria*. In: Bryant, D.A. (Ed.), The Molecular Biology of Cyanobacteria, Advances in Photosynthesis. Springer Netherlands, Dordrecht, pp. 559–579. https://doi.org/10.1007/978-94-011-0227-8_18.

Klughammer, C., Schreiber, U., 1994. An improved method, using saturating light pulses, for the determination of photosystem I quantum yield via $P700^{+}$-absorbance changes at 830 nm. Planta 192, 261–268. https://doi.org/10.1007/BF01089043.

Kremling, K., Pohl, C., 1989. Studies on the spatial and seasonal variability of dissolved cadmium, copper and nickel in northeast atlantic surface waters. Mar. Chem. 27, 43–60. https://doi.org/10.1016/0304-4203(89)90027-3.

Krupnik, T., Kotabová, E., van Bezouwen, L.S., Mazur, R., Garstka, M., Nixon, P.J., Barber, J., Kaňa, R., Boekema, E.J., Kargul, J., 2013. A reaction center-dependent photoprotection mechanism in a highly robust photosystem II from an extremophilic red alga, *Cyanidioschyzon merolae*. J. Biol. Chem. 288, 23529–23542. https://doi.org/10.1074/jbc.M113.484659.

Luca, P.D., Taddei, R., Varano, L., 1978. « *Cyanidioschyzon merolae* »: a new alga of thermal acidic environments. Webbia 33, 37–44. https://doi.org/10.1080/00837792.1978.10670110.

Lundquist, P.K., Poliakov, A., Bhuiyan, N.H., Zybailov, B., Sun, Q., van Wijk, K.J., 2012. The functional network of the *Arabidopsis* plastoglobule proteome based on quantitative proteomics and genome-wide coexpression analysis. Plant Physiol. 158, 1172–1192. https://doi.org/10.1104/pp.111.193144.

Martínez-Ruiz, E.B., Martínez-Jerónimo, F., 2015. Nickel has biochemical, physiological, and structural effects on the green microalga *Ankistrodesmus falcatus*: an integrative study. Aquat. Toxicol. 169, 27–36. https://doi.org/10.1016/j.aquatox.2015.10.007.

Mendoza-Cózatl, D.G., Moreno-Sánchez, R., 2005. Cd^{2+} transport and storage in the chloroplast of *Euglena gracilis*. Biochim. Biophys. Acta Bioenerg. 1706, 88–97. https://doi.org/10.1016/j.bbabio.2004.09.010.

Millach, L., Villagrasa, E., Solé, A., Esteve, I., 2019. Combined confocal laser scanning microscopy techniques for a rapid assessment of the effect and cell viability of *Scenedesmus* sp. DE2009 under metal stress. Microsc. Microanal. Off. J. Microsc. Soc. Am. Microbeam Anal. Soc. Microsc. Soc. Can. 25, 998–1003. https://doi.org/10.1017/S143192761901465X.

Minoda, A., Sakagami, R., Yagisawa, F., Kuroiwa, T., Tanaka, K., 2004. Improvement of culture conditions and evidence for nuclear transformation by homologous recombination in a red alga, *Cyanidioschyzon merolae* 10D. Plant Cell Physiol. 45, 667–671. https://doi.org/10.1093/pcp/pch087.

Miyagishima, S., Wei, J.L., Nozaki, H., Hirooka, S., 2017. *Cyanidiales*: evolution and habitats. In: Kuroiwa, T., Miyagishima, S., Matsunaga, S., Sato, N., Nozaki, H., Tanaka, K., Misumi, O. (Eds.), *Cyanidioschyzon Merolae*: A New Model Eukaryote for Cell and Organelle Biology. Springer Singapore, Singapore, pp. 3–15. https://doi.org/10.1007/978-981-10-6101-1_1.

Miyagishima, S.-Y., Tanaka, K., 2021. The unicellular red alga *Cyanidioschyzon merolae*—the simplest model of a photosynthetic eukaryote. Plant Cell Physiol. 62, 926–941. https://doi.org/10.1093/pcp/pcab052.

Mojaat, M., Pruvost, J., Foucault, A., Legrand, J., 2008. Effect of organic carbon sources and Fe^{2+} ions on growth and β-carotene accumulation by *Dunaliella salina*. Biochem. Eng. J. 39, 177–184. https://doi.org/10.1016/j.bej.2007.09.009.

Monteiro, C.M., Castro, P.M.L., Malcata, F.X., 2012. Metal uptake by microalgae: underlying mechanisms and practical applications. Biotechnol. Prog. 28, 299–311. https://doi.org/10.1002/btpr.1504.

Monteiro, C.M., Fonseca, S.C., Castro, P.M.L., Malcata, F.X., 2011. Toxicity of cadmium and zinc on two microalgae, *Scenedesmus obliquus* and *Desmodesmus pleiomorphus*, from Northern Portugal. J. Appl. Phycol. 23, 97–103. https://doi.org/10.1007/s10811-010-9542-6.

Moran, R., 1982. Formulae for determination of chlorophyllous pigments extracted with N,N-Dimethylformamide. Plant Physiol. 69, 1376–1381. https://doi.org/10.1104/pp.69.6.1376.

Muramoto, S., Brison, J., Castner, D.G., 2012. Exploring the surface sensitivity of ToF-SIMS by measuring the implantation and sampling depths of bin and C60 ions in organic films. Anal. Chem. 84, 365–372. https://doi.org/10.1021/ac202713k.

Nagajyoti, P.C., Lee, K.D., Sreekanth, T.V.M., 2010. Heavy metals, occurrence and toxicity for plants: a review. Environ. Chem. Lett. 8, 199–216. https://doi.org/10.1007/s10311-010-0297-8.

Nagasaka, S., Nishizawa, N.K., Mori, S., Yoshimura, E., 2004. Metal metabolism in the red alga *Cyanidium caldarium* and its relationship to metal tolerance. Biometals 17, 177–181. https://doi.org/10.1023/B:BIOM.0000018403.37716.ff.

Nagasaka, S., Nishizawa, N.K., Negishi, T., Satake, K., Mori, S., Yoshimura, E., 2002. Novel iron-storage particles may play a role in aluminum tolerance of *Cyanidium caldarium*. Planta 215, 399–404. https://doi.org/10.1007/s00425-002-0764-y.

Nowicka, B., 2022. Heavy metal-induced stress in eukaryotic algae-mechanisms of heavy metal toxicity and tolerance with particular emphasis on oxidative stress in exposed cells and the role of antioxidant response. Environ. Sci. Pollut. Res. Int. 29, 16860–16911. https://doi.org/10.1007/s11356-021-18419-w.

OriginLab Corporation, 2018. Origin(Pro), Version 2018b. OriginLab Corporation, Northampton, MA, USA.

Pinto, E., Sigaud-Kutner, T.C.S., Leitão, M.A.S., Okamoto, O.K., Morse, D., Colepicolo, P., 2003. Heavy metal–induced oxidative stress in algae. J. Phycol. 39, 1008–1018. https://doi.org/10.1111/j.0022-3646.2003.02-193.x.

Piochi, M., Mormone, A., Strauss, H., Balassone, G., 2019. The acid sulfate zone and the mineral alteration styles of the Roman Puteoli (Neapolitan area, Italy): clues on fluid fracturing progression at the Campi Flegrei volcano. Solid Earth 10, 1809–1831. https://doi.org/10.5194/se-10-1809-2019.

Raman, A., Muniappan, R., Silva-Krott, I.U., Reddy, G.V.P., 2006. Induced-defense responses in the leaves of *Chromolaena odorata* consequent to infestation by *Pareuchaetes pseudoinsulata* (Lepidoptera: Arctiidae). J. Plant Dis. Prot. 113, 234–239. https://doi.org/10.1007/BF03356187.

Raven, J.A., Beardall, J., Quigg, A., 2020. Light-driven oxygen consumption in the water-water cycles and photorespiration, and light stimulated mitochondrial respiration. In: Larkum, A.W.D., Grossman, A.R., Raven, J.A. (Eds.), Photosynthesis in Algae: Biochemical and Physiological Mechanisms, Advances in Photosynthesis and Respiration. Springer International Publishing, Cham, pp. 161–178. https://doi.org/10.1007/978-3-030-33397-3_8.

Rezayian, M., Niknam, V., Ebrahimzadeh, H., 2019. Oxidative damage and antioxidative system in algae. Toxicol Rep 6, 1309–1313. https://doi.org/10.1016/j.toxrep.2019.10.001.

RStudio Team, 2015. RStudio. Integrated Development Environment for R. RStudio, Inc., Boston, MA.

Santos, F.M., Mazur, L.P., Mayer, D.A., Vilar, V.J.P., Pires, J.C.M., 2019. Inhibition effect of zinc, cadmium, and nickel ions in microalgal growth and nutrient uptake from water: an experimental approach. Chem. Eng. J. 366, 358–367. https://doi.org/10.1016/j.cej.2019.02.080.

Schönwälder, S.M.S., Bally, F., Heinke, L., Azucena, C., Bulut, Ö.D., Heißler, S., Kirschhöfer, F., Gebauer, T.P., Neffe, A.T., Lendlein, A., Brenner-Weiß, G., Lahann, J., Welle, A., Overhage, J., Wöll, C., 2014. Interaction of human plasma proteins with thin gelatin-based hydrogel films: a QCM-D and ToF-SIMS study. Biomacromolecules 15, 2398–2406. https://doi.org/10.1021/bm500750v.

Shahzad, B., Tanveer, M., Rehman, A., Cheema, S.A., Fahad, S., Rehman, S., Sharma, A., 2018. Nickel; whether toxic or essential for plants and environment - a review. Plant Physiol. Biochem. 132, 641–651. https://doi.org/10.1016/j.plaphy.2018.10.014.

Shakhatreh, M.A.K., Jacob, J.H., Hussein, E.I., Masadeh, M.M., Obeidat, S.M., Juhmani, A.F., Abd Al-razaq, M.A., 2017. Microbiological analysis, antimicrobial activity, and heavy-metals content of Jordanian Ma'in hot-springs water. J. Infect. Public Health 10, 789–793. https://doi.org/10.1016/j.jiph.2017.01.010.

Shanab, S., Essa, A., Shalaby, E., 2012. Bioremoval capacity of three heavy metals by some microalgae species (Egyptian Isolates). Plant Signal. Behav. 7, 392–399. https://doi.org/10.4161/psb.19173.

Sharma, S.S., Dietz, K.-J., Mimura, T., 2016. Vacuolar compartmentalization as indispensable component of heavy metal detoxification in plants. Plant Cell Environ. 39, 1112–1126. https://doi.org/10.1111/pce.12706.

Solymosi, K., Mysliwa-Kurdziel, B., 2021. The role of membranes and lipid-protein interactions in the Mg-branch of tetrapyrrole biosynthesis. Front. Plant Sci. 12.

Szalontai, B., Nishiyama, Y., Gombos, Z., Murata, N., 1999. Membrane dynamics studied by FTIR spectroscopy in thylakoid and cytoplasmic membranes of *Synechocystis* PCC6803. Lipids and the effect of protein to lipid ratios. In: Greve, J., Puppels, G.J., Otto, C. (Eds.), Spectroscopy of Biological Molecules: New Directions: 8th European Conference on the Spectroscopy of Biological Molecules, 29 August–2 September 1999, Enschede, The Netherlands. Springer Netherlands, Dordrecht, pp. 385–386. https://doi.org/10.1007/978-94-011-4479-7_172.

Thiruvallur Eachambadi, R., Boschker, H.T.S., Franquet, A., Spampinato, V., Hidalgo-Martinez, S., Valcke, R., Meysman, F.J.R., Manca, J.V., 2021. Enhanced laterally resolved ToF-SIMS and AFM imaging of the electrically conductive structures in cable bacteria. Anal. Chem. 93, 7226–7234. https://doi.org/10.1021/acs.analchem.1c00298.

Varshney, P., Mikulic, P., Vonshak, A., Beardall, J., Wangikar, P.P., 2015. Extremophilic micro-algae and their potential contribution in biotechnology. Bioresour. Technol. 184, 363–372. https://doi.org/10.1016/j.biortech.2014.11.040.

Venzhik, YuV., Shchyogolev, S.Yu, Dykman, L.A., 2019. Ultrastructural reorganization of chloroplasts during plant adaptation to abiotic stress factors. Russ. J. Plant Physiol. 66, 850–863. https://doi.org/10.1134/S102144371906013X.

Wellburn, A.R., 1994. The spectral determination of chlorophylls a and b, as well as total carotenoids, using various solvents with spectrophotometers of different resolution. J. Plant Physiol. 144, 307–313. https://doi.org/10.1016/S0176-1617(11)81192-2.

Yagisawa, F., Nishida, K., Yoshida, M., Ohnuma, M., Shimada, T., Fujiwara, T., et al., 2009. Identification of novel proteins in isolated polyphosphate vacuoles in the primitive red alga *Cyanidioschyzon merolae*. Plant J. 60, 882–893. https://doi.org/10.1111/j.1365-313X.2009.04008.x.

Zhang, R., Wise, R.R., Struck, K.R., Sharkey, T.D., 2010. Moderate heat stress of *Arabidopsis thaliana* leaves causes chloroplast swelling and plastoglobule formation. Photosynth. Res. 105, 123–134. https://doi.org/10.1007/s11120-010-9572-6.

Zheng, Q., Cheng, Z.Z., Yang, Z.M., 2013. HISN3 mediates adaptive response of *Chlamydomonas reinhardtii* to excess nickel. Plant Cell Physiol. 54, 1951–1962. https://doi.org/10.1093/pcp/pct130.